



SAPIENZA  
UNIVERSITÀ DI ROMA

# Majorana Fermions at Self Generated Interfaces

Facoltà di Scienze Matematiche Fisiche e Naturali  
Fisica

**Nikola Prodanov**

ID number 1768690

Advisors

Prof. Sergio Caprara

Prof. Sergio Ciuchi

Academic Year 2024/2025

Thesis not yet defended

---

**Majorana Fermions at Self Generated Interfaces**  
Sapienza University of Rome

© 2024 Nikola Prodanov. All rights reserved

This thesis has been typeset by L<sup>A</sup>T<sub>E</sub>X and the Sapthesis class.

Author's email: [nikola.prodanov2023@gmail.com](mailto:nikola.prodanov2023@gmail.com)

## Abstract

The quasiparticle Majorana fermion in one-dimensional condensed matter systems typically appears at the edges of a topological chain or at the interface between distinct topological phases. Constructing such systems is challenging, requiring carefully tuned conditions and the combination of different materials. One of the simplest one-dimensional models, the Kitaev chain, exhibits two distinct phases at varying electron densities: a non-topological homogeneous phase and a topological homogeneous phase, with no coexistence between them. Introducing an external classical elastic field, coupled to the electron density at each site in the Kitaev model, leads to the emergence of a coexisting phase between these two homogeneous phases as the coupling strength increases. Furthermore, this coupling leads to the emergence of additional phases, including non-topological charge density waves, which can coexist with the topological homogeneous phase. These coexisting regions have the potential to host Majorana fermions.

# Acknowledgments

*To be written when everything is over...*

# Contents

<b>Introduction</b>	<b>1</b>
<b>1 Topology and Majorana Fermions in Superconductors</b>	<b>5</b>
1.1 Topology in Condensed Matter Systems . . . . .	6
1.2 Fermion Operators and Majorana Operators . . . . .	7
1.3 The Kitaev model . . . . .	8
1.3.1 Zero mode Majorana fermions . . . . .	9
1.3.2 The role of the parity symmetry on the ground state . . . . .	11
1.3.3 Topological Protection of the Zero Modes . . . . .	13
1.4 Majorana modes appearing at a domain wall between different phases	16
<b>2 Coupling The Kitaev Model to a Classical Elastic Field at Half Filling</b>	<b>18</b>
2.1 The Hamiltonian . . . . .	18
2.1.1 Emerging New Phase . . . . .	19
2.2 Phase Diagram at Half Filling . . . . .	20
2.2.1 Breaking of the Particle-Hole Symmetry . . . . .	20
2.2.2 Description of the System in Reciprocal Space . . . . .	21
2.2.3 The phase transition . . . . .	25
2.3 The Zero Modes Persist . . . . .	27
<b>3 The Model Away from Half Filling</b>	<b>28</b>
3.1 Peierls Instability and CDWs . . . . .	29
3.1.1 Susceptibility of the Kitaev Model . . . . .	29
3.1.2 Random Phase Approximation Approach . . . . .	33
3.2 Responses to Changing Electron Density . . . . .	36
3.2.1 The Minimization of the Helmholtz Free Energy . . . . .	36
3.2.2 Solutions to Minimization equations . . . . .	37
<b>4 Majorana Zero Modes in the Model</b>	<b>40</b>
4.1 The Phase Diagrams . . . . .	40
4.2 Majorana Fermions in Single Phases . . . . .	43
4.3 Majorana Fermions at Interfaces of Coexisting Phases . . . . .	44
4.3.1 Non-Topo-Homogeneous and Topo-Homogeneous Coexistence	46
4.3.2 Non-Topo-Dimerized and Topo-Homogeneous Coexistence . .	48
<b>Conclusions</b>	<b>50</b>
<b>Appendix</b>	<b>52</b>
<b>Bibliography</b>	<b>55</b>

# Introduction

One of the key areas of study in condensed matter physics is the behavior, dynamics, interactions, and collective phenomena of electrons within various materials. Physicists have developed mathematical descriptions and physical interpretations of electrons and their counterpart holes, treating them as distinct entities. A hole behaves as if it were a particle, moving through the lattice and interacting with other particles similarly to an electron. An electron is considered a carrier of charge  $-e$ , while a hole, representing the absence of an electron, is a carrier of charge  $+e$ . Nothing stops us from considering a quantum state that is a superposition of an electron and a hole, creating a charge-neutral state that is its own antiparticle. This is what condensed matter physicists, since the early 2000s, refer to as a quasi-particle Majorana fermion.

The theory of Majorana fermions<sup>[1]</sup> has been around for nearly a century, but there has not been a confirmed detection of an elementary particle that is its own antiparticle in particle physics<sup>1</sup>[2]. Condensed matter physicists take a different approach, rather than seeking them as elementary particles, they explore quasi-particle Majorana fermions, just like the description of the charge-neutral state superposition of an electron and a hole. These kind of Majorana fermions are expected to be found in topological superconductors.

Topological superconductors<sup>[3]</sup> are a special class of materials where superconductivity coexists with non-trivial topological properties. Unlike conventional superconductors, which are characterized solely by their ability to conduct electricity without resistance below a critical temperature, topological superconductors exhibit unique electronic states protected by topology. This protection by topology is a specific mathematical characteristics of the electronic band structures or wave functions. These characteristics are quantified by numerical values, called the topological invariant or criterion<sup>[4]</sup>, that classify different topological phases of the material. It also means that as long as the material remains within the same topological phase (characterized by the same topological invariant), certain electronic states or properties will be robust against disorder, defects, or other types of perturbations that do not change the topological nature of the material.

Research into topological superconductors isn't solely driven by theoretical exploration and the study of new phases of matter. It aims to harness these materials directly for quantum computation, seeking to leverage their promising characteristics to avoid challenges faced by current quantum computers<sup>[5]</sup>. Essentially they use the topological protection in the system. Consider quantum bits in conventional quantum computing, they are susceptible to errors from environmental noise and disturbances. However, quantum bits based on topological protection are inherently more stable because their quantum states are protected by the topology of the material rather than relying solely on fragile quantum coherence times. This protection makes them

---

<sup>1</sup>Particle physicists have faith in neutrinos, hoping that observing a neutrinoless double-beta decay will prove their hypothesis that neutrinos are Majorana fermions.

completely independent to errors caused by local perturbations.

Over the past decade, numerous efforts have been made to detect Majorana fermions in topological superconductors. Theoretical approaches predict finding them in several configurations of topological superconductors. One of the most widely studied experimental signatures of Majorana fermions is in nanowire systems [6]-[12], i.e., observing the zero-bias conductance peak. This feature is observed in differential conductance measurements when a material system containing a superconductor and a semiconductor exhibits a conductance peak at zero voltage. The conductance should be quantized at  $2e^2/h$  due to the topological protection of the Majorana state. An example is shown in Fig. 0.1, where a result from a research group observed signals that led them to interpret the results as a zero-bias conductance peak consistent with theoretical predictions for Majorana fermions. However, the interpretation of zero-bias conductance peak results came under debate

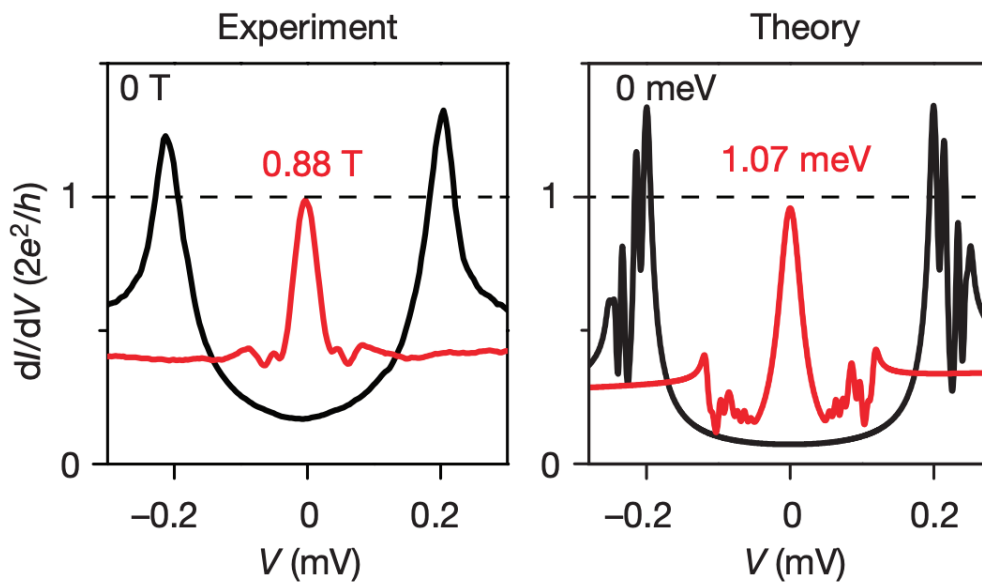


**Figure 0.1.** From [13]. The experimental zero-voltage peak (see left figure), which is a theoretical prediction (see right figure), was considered a potential signature of Majorana zero modes. This is a 2018 paper that claimed the discovery of Majorana fermions which was later retracted in 2021 due to flaws in data analysis[14].

in the following years, and it became understood within the scientific community that such signals could also arise from alternative mechanisms, such as trivial Andreev bound states, interface disorder, or strong magnetic fields generating non-topological low-energy states. These findings ultimately cast doubt on the original interpretation and serve as a reminder of the complexity and depth involved in the search for Majorana fermions in such systems.

Another approach in the search for Majorana fermions involves scanning tunneling microscopy studies of vortex cores in superconductors [15]-[16]. These studies have reported zero-bias peaks, initially seen as evidence of Majorana zero modes. However, similar signals can result from trivial Caroli-de Gennes-Matricon states [17], disorder effects, and vortex interactions, leading to uncertainty in their interpretation.

While the scientific community is researching and conducting experiments on the detection of these quasiparticles, Microsoft Corporation announced its latest processor, *Majorana 1*, see Fig. 0.2.

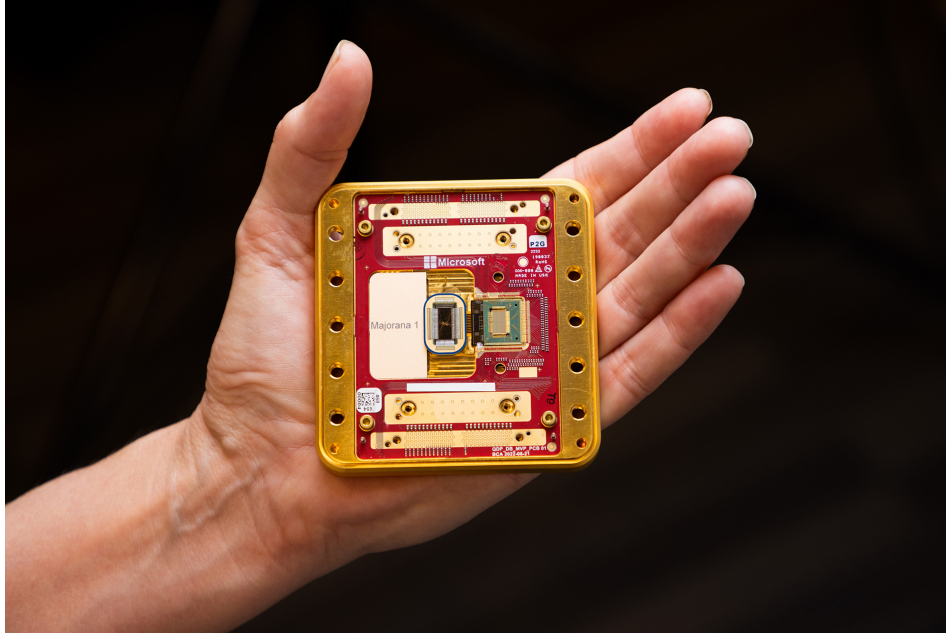


**Figure 0.2.** From [18]. Microsoft Corporation unveiled its *Majorana 1* processor on February 19, 2025, with the announcement: "...the world's first quantum processor powered by topological qubits."

The wording that Microsoft uses may lead the reader and the media to believe that the existence of Majorana fermions has been definitively proven, as the processor is claimed to be based on them. The unveiling of *Majorana 1* fermions coincided with a paper [19] published in *Nature* by Microsoft's Azure Quantum researchers, describing the device's properties. The peer review report on the paper states:

*"The editorial team wishes to point out that the results in this manuscript do not represent evidence for the presence of Majorana zero modes in the reported devices. The work is published for introducing a device architecture that might enable fusion experiments using future Majorana zero modes."*

- *Nature*, Peer review on [19]

Microsoft's team claims that the research presented in this paper is now outdated, asserting that since its submission in March 2024, they have successfully implemented topological qubits in basic operations. However, as of the defense date of this thesis, no scientific paper has definitively proven the detection of Majorana fermions as quasiparticles in condensed matter physics, though physicists continue their slow, ongoing theoretical and experimental research while eagerly awaiting their detection.

On the theoretical front, there have been advancements in designing experiments aimed at detecting Majorana fermions. One recent example involves studying the behavior of the DC Josephson current [20] in a junction between a trivial and a topological superconductor [21], demonstrating how Majorana fermions influence the supercurrent in such systems. Meanwhile, on the experimental side, significant progress [22] has been made toward realizing the Kitaev model [23], which originally



inspired the scientific community's search for Majorana fermions. In this thesis, we aim to contribute to this model by presenting our own theoretical advancements. The Chapters of the thesis are structured as follows:

- In Chapter One, we provide a brief introduction to topology and topological superconductors. We introduce the simplest model of a topological superconductor, namely the Kitaev model, and present all its significant results, culminating in the emergence of zero-mode Majorana edge states. Additionally, we explore the theoretical aspects of detecting Majorana fermions at the junctions between different topological phases.
- In Chapter Two, we introduce the classical elastic field coupled to the electrons of the Kitaev model. We demonstrate that under specific parameters of the Hamiltonian, even as a small perturbation, this external field can break the symmetry of the system. This alteration in symmetry results in a change in the system's topology, leading to the emergence of a new phase, a charge density wave. Consequently, we construct a phase diagram at half filling that delineates the transition between these two phases.
- In Chapter Three, we investigate the model at various electron densities. We derive an equation that guides us in preventing the formation of charge density waves, as their topological nature is not of our interest. Additionally, we demonstrate how the classical elastic field creates a region where topological and non-topological phases can coexist. Unlike the original Kitaev model.
- In Chapter Four, we utilize the theoretical findings from Chapter Three to construct phase diagrams at various electron densities. Finally, computational methods confirm the localization of distinct Majorana fermions at the interfaces of different topological phases within the coexisting region.

## Chapter 1

# Topology and Majorana Fermions in Superconductors

Topology[24] is a branch of mathematics that studies properties of geometrical objects that remain unchanged under continuous deformations such as stretching or bending. These properties are insensitive to smooth transformations and provide a powerful framework for understanding complex structures. One of the simplest examples involves closed two-dimensional surfaces in three-dimensional space: for instance, a sphere can be smoothly deformed into various shapes like the surface of a disk or a bowl, but it cannot be smoothly deformed into a torus (doughnut). The key distinction lies in an integer topological invariant known as the genus  $g$ , which counts the number of holes in the surface. Since the genus is an integer, it cannot change through smooth deformations, making surfaces with different genus topologically distinct, see Figure 1.1. Surfaces with the same genus are topologically equivalent and can be smoothly transformed into each other.

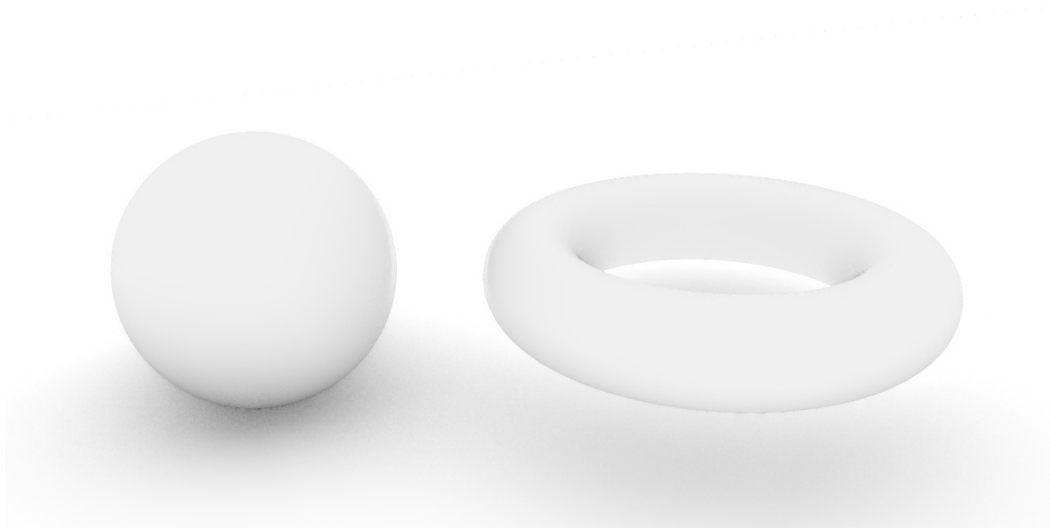


**Figure 1.1.** The sphere on the left has a genus, or number of holes,  $g = 0$ . The Torus (doughnut) on the right side has a genus  $g = 1$ . These two objects cannot be smoothly transformed into each other.

Identifying the topological invariants of an object is a fascinating mathematical challenge. Topology in condensed matter physics involves studying whether two

quantum systems can be continuously transformed into one another. If they can, the systems are considered topologically equivalent. But what would be the equivalent of the topological invariant genus for a quantum system?

## 1.1 Topology in Condensed Matter Systems

In condensed matter physics, we can examine whether the Hamiltonians of two quantum systems can be continuously transformed into each other. If such a continuous transformation is possible, we say that the two systems are topologically equivalent. If we considered all Hamiltonians without any constraint, every Hamiltonian could be continuously deformed into every other Hamiltonian, and all quantum systems would be topologically equivalent. An example of such a smooth path can be parameterized by  $t \in [0, 1]$  to connect two different Hamiltonians  $H$  and  $H'$  in the following manner:

$$H(t) = tH' + (1 - t)H \quad (1.1)$$

This changes drastically if we restrict ourselves to systems with certain properties, for example an energy gap, i.e., insulators.

An insulator is a material that has an energy gap for electronic excitations, which separates the ground state from all excited states. This allows for a notion of topological equivalence based on the principle of adiabatic continuity. Insulators are equivalent if they can be changed into one another by slowly changing the Hamiltonian, such that the system always remains in the ground state. Such a process is possible if there is an energy gap, which sets a scale for how slow the adiabatic process must be. Thus, insulators are topologically equivalent if there exists an adiabatic path, equivalent to or significantly more complex than (1.1), connecting them along which the energy gap remains finite. It follows that connecting topologically nonequivalent insulators necessarily involves a phase transition, in which the energy gap vanishes, see Figure 1.2:



**Figure 1.2.** This figure highlights the main difference in the energy band structures between an insulator (left) and a conductor (right). The insulator exhibits a significant energy gap between the valence band and the conduction band, preventing electron flow. If the energy gap narrows and ultimately closes the system undergoes a phase transition into a conductor. This allows the electrons to flow between the valence and conduction band at finite temperatures. Otherwise, at  $T = 0K$ , the conduction band is empty.

This motivates us to introduce the concept of a topological criterion which, in this case for insulators would be defined as: two insulators are topologically equivalent

if their Hamiltonians can be continuously deformed into each other without ever closing the energy gap.

So in condensed matter physics, two quantum systems are considered topologically equivalent if there exists a continuous path from Hamiltonian  $H$  to Hamiltonian  $H'$  that preserves a specific topological criterion. If no such path can be constructed while conserving this topological criterion, the systems are considered topologically nonequivalent, indicating that a phase transition must occur along that path. The complexity of topology arises from the task of establishing whether there exists at least one path connecting two Hamiltonians while conserving the topological criterion. In this thesis, we focus on exploring a topological superconducting system capable of hosting Majorana Fermions (MFs). Specifically, we aim for our topological criterion to manifest as the presence of zero-mode Majoranas. To explore this, we first introduce in this chapter the Kitaev toy model, one of the simplest models of a topological superconductors. However, before we do that, let's revisit in the next section the theory and notation of MFs.

## 1.2 Fermion Operators and Majorana Operators

Ettore Majorana, an Italian physicist, made groundbreaking contributions to theoretical physics in the early 20th century. Among his notable achievements was the prediction of a new class of particles that would later bear his name: Majorana fermions. In 1937, Majorana proposed the existence of fermion particles that are their own antiparticles, introducing a concept that would profoundly influence both theoretical and experimental physics.

To understand MFs, it's essential to first grasp the basics of fermion operators. In quantum mechanics, fermions are particles that obey the Pauli exclusion principle, necessitating the use of anticommutation relations for their operators. Consider a fermion creation operator  $c_l^\dagger$  that creates a fermion in a generic state  $l$ , e.g., a Wannier state centered on site  $l$ , and its corresponding annihilation operator  $c_l$ . These operators satisfy the canonical anticommutation relations  $\{c_l, c_m^\dagger\} = \delta_{lm}$  and, furthermore, square to zero,  $(c_l)^2 = 0$  and  $(c_l^\dagger)^2 = 0$ . They are the bridge between two states  $|0\rangle$  and  $|1\rangle$  which correspond to the vacuum with no particle and the excited state with one particle, according to the following rules defined  $c_l |0\rangle = 0$ ,  $c_l^\dagger |0\rangle = |1\rangle$  and  $c_l^\dagger |1\rangle = 0$ .

Now, let's introduce Majorana operators. A MF operator can be expressed as a linear combination of fermion operators as follows:

$$\gamma_{A,l} = \frac{1}{i\sqrt{2}}(c_l - c_l^\dagger) \quad \gamma_{B,l} = \frac{1}{\sqrt{2}}(c_l + c_l^\dagger) \quad (1.2)$$

Notice the similarity with the operator definitions of position  $x$  and momentum  $p$  for the harmonic oscillator [25]. Just like the position and momentum operators, the  $\gamma$  operators are as well hermitian:

$$\gamma^\dagger = \gamma \quad (1.3)$$

This last equation implies that the act of creating a particle is indistinguishable from the act of annihilating an antiparticle. In other words, applying the creation operator  $\gamma^\dagger$  creates a particle, and applying the annihilation operator  $\gamma$  destroys a particle, but there's no distinction between creating a particle or destroying an antiparticle. This symmetry between particle creation and antiparticle annihilation

suggests that MFs are their own antiparticles. Another useful property that arises from (1.2) is:

$$\{\gamma_A, \gamma_B\} = 0, \quad \gamma_A^2 = \frac{1}{2}, \quad \gamma_B^2 = \frac{1}{2} \quad (1.4)$$

Majorana operators inherently come in pairs. This pairing is essential for maintaining the fermion character of the operators and ensuring that they satisfy the appropriate anticommutation relations. In condensed matter systems, Majorana modes typically emerge at the boundaries of topological superconductors or at defect sites, where each Majorana mode is paired with another to form a composite fermion excitation. In topological superconductors, for instance, Majorana bound states at the ends of a one dimensional chain come in pairs, with one mode localized at each end. One of the simplest example of this chain is the Kitaev Model.

### 1.3 The Kitaev model

The Kitaev model was introduced by Alexei Kitaev, a Russian–American physicist, in 2001 as a tractable example to study topological superconductivity and MFs.

In the one-dimensional Kitaev chain, the system consists of a linear chain of  $N$  lattice sites with spacing  $a$ , where each site can host a single spinless fermion. The spin degree of freedom can be effectively frozen, for instance, under the influence of a strong magnetic field or due to significant spin-orbit coupling, which allows for the simplification of the problem. The Hamiltonian for this system can be written as:

$$H = -t \sum_{l=0}^{N-1} (c_l^\dagger c_{l+1} + c_{l+1}^\dagger c_l) + \Delta \sum_{l=0}^{N-1} (c_l^\dagger c_{l+1}^\dagger + c_{l+1} c_l) - \mu \sum_{l=0}^{N-1} c_l^\dagger c_l \quad (1.5)$$

Here,  $c_l$  and  $c_l^\dagger$  are fermion annihilation and creation operators at site  $l$ , respectively. The first term represents hopping of fermions between nearest-neighboring sites with hopping amplitude  $t$ . The second term involves a proximity-induced superconducting pairing with strength  $\Delta$ , which represents the p-wave pairing amplitude and arises from the coupling to a superconducting substrate. The last term is the chemical potential term  $\mu$ , which controls the filling of the lattice.

Superconducting Hamiltonians, such as (1.5), can be generalized in the form:

$$H = \sum_{n,m} \left( h_{nm} c_n^\dagger c_m + \Delta_{nm} c_n^\dagger c_m^\dagger + \Delta_{nm}^* c_m c_n \right) \quad (1.6)$$

where the indices  $n$  and  $m$  are integers varying from 0 to  $N - 1$ . This last form can be written compactly in the Bogoljubov-de Gennes form [26]:

$$H = \Psi^\dagger H_{\text{BdG}} \Psi \quad (1.7)$$

where all the creation and annihilation operators have been grouped in a single vector, called the Nambu vector [27],  $\Psi^\dagger = (c_0^\dagger, \dots, c_{N-1}^\dagger, c_0, \dots, c_{N-1})$  and the Hamiltonian  $H_{\text{BdG}}$  is a  $2N \times 2N$  matrix of the following structure:

$$H_{\text{BdG}} = \begin{pmatrix} h & \Delta \\ \Delta^* & -h^* \end{pmatrix} \quad (1.8)$$

Here  $h$  and  $\Delta$  are  $N \times N$  matrices, containing terms  $h_{nm}$  and  $\Delta_{nm}$ , respectively, defined in equation (1.6). The Bogoliubov-de Gennes Hamiltonian operates on

wave functions where the first half consists of electron annihilation operators, and the second half consists of the corresponding electron creation operators. This construction effectively doubles the degrees of freedom in the system by introducing an extra set of hole states.

Due to the relationship between electrons and holes,  $H_{\text{BdG}}$  exhibits a symmetry that exchanges electrons and holes. This symmetry is represented by an anti-unitary operator  $\mathcal{P} = \sigma_x \otimes \mathcal{K}$ , where  $\sigma_x$  is the  $x$  Pauli matrix acting on the particle and hole blocks, and  $\mathcal{K}$  is the complex conjugation operator, see more in [28]. We have that:

$$\mathcal{P}H_{\text{BdG}}\mathcal{P}^{-1} = -H_{\text{BdG}} \quad (1.9)$$

This demonstrates that particle-hole symmetry is represented by an anti-unitary operator that anti-commutes with the Hamiltonian. Due to the negative sign in equation (1.9), the spectrum of  $H_{\text{BdG}}$  must be symmetric with respect to zero energy. Specifically, if there exists an eigenvector  $\Psi$  with an eigenvalue  $E$ , it implies that there will always exist a particle-hole symmetric eigenvector  $\mathcal{P}\Psi$  with eigenvalue  $-E$ :

$$H_{\text{BdG}}\mathcal{P}\Psi = -\mathcal{P}H_{\text{BdG}}\Psi = -E\mathcal{P}\Psi \quad (1.10)$$

As discussed in the section (1.1) examining the energy spectrum provides significant insight into how the topology of the system changes, including identifying phase transitions. However, analyzing the spectrum and the phases of the Kitaev model is challenging in real space. Therefore, in the following discussion, we will build on Kitaev's work by outlining the conditions for the two phases of the Kitaev model, and later give a deeper understanding from the perspective of the momentum space.

### 1.3.1 Zero mode Majorana fermions

To elucidate the two topologically distinct phases, Kitaev transformed the fermion operators into Majorana operators, as delineated in (1.2). This transformation yields the Hamiltonian (1.5) in real space:

$$H = -\mu \sum_{l=0}^{N-1} \left( \frac{1}{2} + i\gamma_{B,l}\gamma_{A,l} \right) - i \sum_{l=0}^{N-2} \left[ (\Delta + t)\gamma_{B,l}\gamma_{A,l+1} + (\Delta - t)\gamma_{A,l}\gamma_{B,l+1} \right] \quad (1.11)$$

The Hamiltonian (1.11) expressed in terms of MF operators suggests that the system's configuration will vary depending on the chosen parameters, leading to different types of pairings of the Majoranas. These pairings can be illustrated with the use of domino tiles, see Figure 1.3.

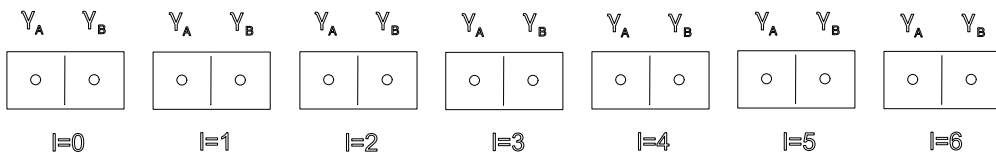


**Figure 1.3.** This figure illustrates the Hamiltonian (1.11) with  $N = 7$  sites, represented using domino tiles. Each site  $l$  is depicted by a domino tile, with each tile hosting two MFs,  $\gamma_A$  and  $\gamma_B$ .

Initially, let's consider a set of parameters  $\mu < 0$ ,  $\Delta = 0$ , and  $t = 0$ . In this scenario, the Hamiltonian takes the form:

$$H = -\mu \sum_{l=0}^{N-1} \left( \frac{1}{2} + i\gamma_{B,l}\gamma_{A,l} \right) \quad (1.12)$$

In which MFs are paired on the same site. This configuration, depicted in Figure 1.4, does not leave any unpaired Majoranas.

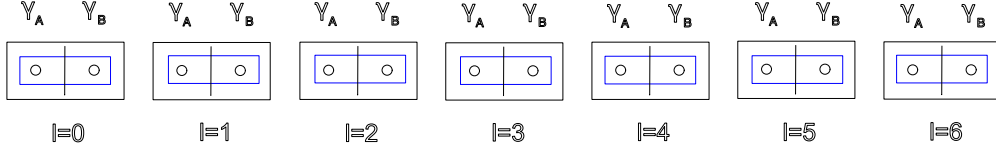


**Figure 1.4.** Illustration of the pairing of the MFs in Hamiltonian (1.12) for  $N = 7$  sites. There are no unpaired MFs in this configuration.

If we took a different set of parameters  $\mu = 0$ ,  $\Delta = t$ , and  $t > 0$ . The Hamiltonian would take a different form:

$$H = -2it \sum_{l=0}^{N-2} \gamma_{B,l}\gamma_{A,l+1} \quad (1.13)$$

Here the Majorana operators  $\gamma_{B,l}\gamma_{A,l+1}$  from different sites are paired together, see Figure 1.5.

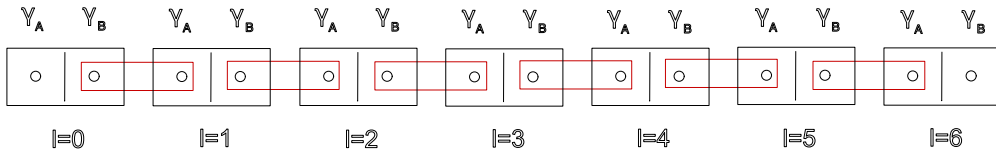


**Figure 1.5.** Illustration of the pairing of the MFs in Hamiltonian (1.13) for  $N = 7$  sites. The MFs at the edges remain unpaired!

Notice how, while all pairs of  $(\gamma_{B,l}, \gamma_{A,l+1})$  for  $l = 0, 1, \dots, N-2$  form new Dirac fermions,  $\gamma_{A,0}$  and  $\gamma_{B,N-1}$  are non appearing in the Hamiltonian (1.13). This is a crucial fact that will allow the chain to host two zero-energy states, localized at its ends. This holds true when the chain has open boundary conditions, as the two end MFs are unpaired and therefore do not annihilate each other. However, with closed boundary conditions, the two end MFs  $\gamma_{A,0}$  and  $\gamma_{B,N-1}$  would annihilate each other, making it impossible to observe any MF (refer to figure 1.6 for further clarification). The new Dirac fermions can be defined as a linear transformation of the two MFs  $\gamma_{B,l}$  and  $\gamma_{A,l+1}$

$$d_l = \frac{1}{\sqrt{2}}(\gamma_{A,l+1} + i\gamma_{B,l}), \quad l = 0, 1, \dots, N-2 \quad (1.14)$$

Meanwhile the two non appearing MFs  $\gamma_{A,0}$  and  $\gamma_{B,N-1}$  can be collected in a non-local Dirac fermion

$$d = \frac{1}{\sqrt{2}}(\gamma_{A,0} + i\gamma_{B,N-1}) \quad (1.15)$$

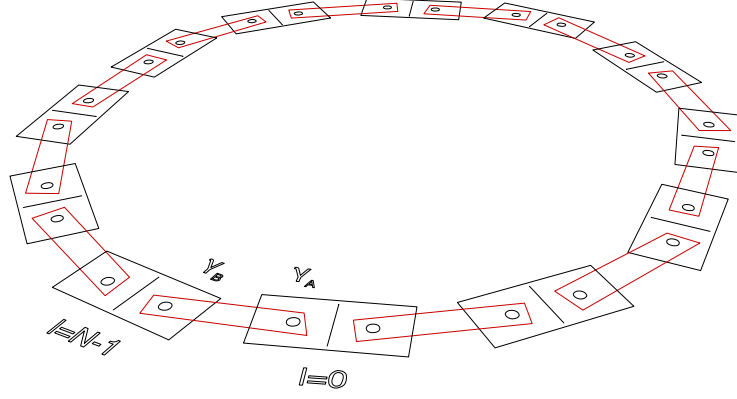


**Figure 1.6.** This is a two-dimensional representation of a one-dimensional Hamiltonian (1.13) with closed boundary conditions. In this configuration,  $\gamma_{A,0}$  and  $\gamma_{B,N-1}$  are adjacent and can be paired together, preventing the system from hosting unpaired MFs under closed boundary conditions.

The Hamiltonian (1.13) becomes

$$H = 2t \sum_{l=0}^{N-2} \left( d_l^\dagger d_l - \frac{1}{2} \right) \quad (1.16)$$

There are two degenerate ground states  $|g_1\rangle$  and  $|g_2\rangle$  defined by the condition  $d_l |g\rangle = 0$  for  $l = 0, 1, \dots, N-2$  with opposite parity, see the following discussion.

### 1.3.2 The role of the parity symmetry on the ground state

In general, the parity operator measures if the number of occupied states, in this case the number of spinless fermions, is even or odd. It is usually defined as

$$P = \prod_l (1 - 2c_l^\dagger c_l) \quad (1.17)$$

where the multiplication is over all the sites of the chain. Given the fact that we encounter only expectation values of  $\langle 0_l | c_l^\dagger c_l | 0_l \rangle$  and  $\langle 1_l | c_l^\dagger c_l | 1_l \rangle$  that respectively take values 0 for the absence of a fermion at the  $l$ -th site and 1 for the presence of a fermion at the  $l$ -th site then the parity operator can only take the following eigenvalues:

$$P = \begin{cases} +1 & \text{if there are an even number of fermions} \\ -1 & \text{if there are an odd number of fermions} \end{cases} \quad (1.18)$$

For the case of (1.16) the parity operator can be written as

$$P = \left[ \prod_{l=0}^{N-2} (1 - 2d_l^\dagger d_l) \right] \cdot (1 - 2d^\dagger d) \quad (1.19)$$



Now, the ground state  $|g_1\rangle$  can be defined as the one with no particles, i.e.,  $d_l |g_1\rangle = 0$  for  $l = 0, 1, \dots, N-2$  and  $d |g_1\rangle = 0$ . Another interesting state is a state that hosts a zero energy fermion  $|g_2\rangle = d^\dagger |g_1\rangle$ . Using the parity operator referenced in (1.19), we apply it to the two states to obtain:

$$\begin{cases} P |g_1\rangle = |g_1\rangle \\ P |g_2\rangle = (1 - d^\dagger d) |g_2\rangle = -|g_2\rangle \end{cases} \quad (1.20)$$

This implies that  $|g_1\rangle$  possesses an even fermion parity, whereas  $|g_2\rangle$  exhibits an odd fermion parity. Similarly, it can be demonstrated that applying the two states  $|g_i\rangle$  to the Hamiltonian (1.16) yields the same ground state energy, i.e.,  $H |g_i\rangle = -t(N-1) |g_i\rangle$ . This is a degeneracy of the ground state. This will be the foundation of our definition of the topological criterion, see the following discussion.

### Defining the Topological Criterion

In previous discussions, we demonstrated that the Kitaev Model exhibits two distinct phases. The first phase has no unpaired MFs, while the second phase features two unpaired MFs at the edges of the chain, both occupying the same zero-modes. We will distinguish these two phases by considering a topological criterion, defined as follows: A phase is considered topological if the criterion of the Kitaev Model is satisfied, meaning the system exhibits a ground state degeneracy corresponding to the presence of zero-mode Majoranas. Otherwise the phase will be considered non-topological.

This definition of the topological criterion is still very general and it doesn't tell us for a given set of parameters  $\mu$ ,  $\Delta$  and  $t$  if the system constructs a topological or non-topological phase. A numerical diagonalization of the Hamiltonian (1.5) at fixed  $\Delta$  and  $t$ , while varying  $\mu$ , shows us that the zero-modes persist up to values of  $|\mu| \simeq 2t$ , see Figure 1.7.

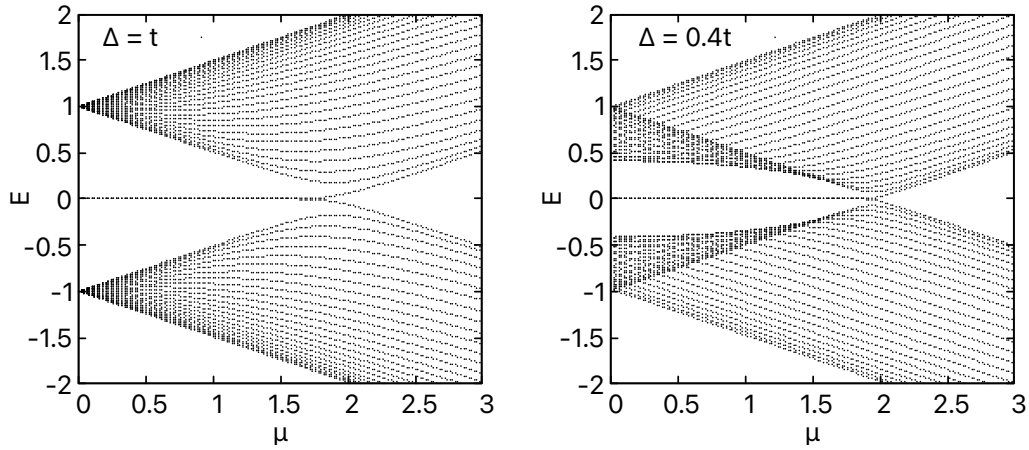


**Figure 1.7.** Energy spectrum vs the chemical potential  $\mu$ . Here  $N = 25$  and  $t = 1$ . The figure on the left is for  $\Delta = t$ . The figure on the right is for  $\Delta = 0.4t$ . Both figures show that the zero modes split when  $\mu \simeq 2t$ .

These figures hint that the boundary of the topological phase is  $\mu \simeq 2t$ . To understand the physical meaning of this topological boundary, we will analyze the energy spectrum analytically in momentum space in the next section.

### 1.3.3 Topological Protection of the Zero Modes

Understanding the two phases with distinct topology becomes clearer when transitioning to the momentum space of the Hamiltonian and examining the resulting spectrum. The Hamiltonian (1.5) can also be written in the Bogoljubov-de Gennes form in momentum space. Let's introduce the Fourier transform of the operators in momentum space:

$$c_l = \frac{1}{\sqrt{N}} \sum_{j=0}^{N-1} c_{k_j} e^{-ik_j \cdot x_l} \quad (1.21)$$

$$c_l^\dagger = \frac{1}{\sqrt{N}} \sum_{j=0}^{N-1} c_{k_j}^\dagger e^{ik_j \cdot x_l} \quad (1.22)$$

Here,  $x$  takes discrete  $x_l = la$  values for  $l = 0, 1, \dots, N-1$ . Meanwhile  $k$  is the momentum variable, where  $k_j = \frac{2\pi j}{Na}$  for  $j = 0, 1, \dots, N-1$ . Notice that in this last definition of  $k$  we have applied the periodic boundary conditions: this means that values of  $k$  which differ by  $2\pi/a$  are equivalent. One can also imagine that for large  $N$ ,  $k$  is a continuous periodic variable with values in the interval  $[-\frac{\pi}{a}, \frac{\pi}{a}]$ , the Brillouin zone. Substituting these expressions into the Hamiltonian, we obtain:

$$H = \sum_k \left[ (-2t \cos(ka) - \mu) c_k^\dagger c_k + \Delta c_k^\dagger c_{-k}^\dagger e^{-ika} + \Delta c_{-k} c_k e^{ika} \right] \quad (1.23)$$

Utilizing the commutation and anticommutation relations of the annihilation and creation operators for fermions, the Hamiltonian can be elegantly expressed in the Bogoliubov-de Gennes form:

$$H = \sum_k \Psi_k^\dagger \begin{pmatrix} \xi_k & i\Delta_k \\ -i\Delta_k & -\xi_k \end{pmatrix} \Psi_k - \mu \frac{N}{2} \quad (1.24)$$

In this last equation,  $\Psi_k^\dagger = (c_k^\dagger \ c_{-k})$  is the Nambu vector for spinless fermions in momentum space. Also  $\xi_k = -t \cos(ka) - \mu/2$  and  $\Delta_k = \Delta \sin(ka)$ . We diagonalize the  $2 \times 2$  matrix within the Bogoljubov-de Gennes form to obtain the band structure of the Kitaev chain, that is the energy levels  $E_k$ :

$$E_k = \pm \sqrt{\xi_k^2 + \Delta_k^2} \quad (1.25)$$

The energy spectrum for fixed values of  $\Delta$  and  $t$  as  $\mu$  varies is shown in Figures 1.8: In these figures, zero-mode Majoranas are absent due to the application of closed boundary conditions, which inherently eliminate any Majorana edge states, recall Figure 1.6. We use this approach because the spectrum for closed and open boundary conditions is identical, except for the presence of zero modes.

Here,  $\Delta = 0.4t$ . One can analytically prove, using the same approach to obtain equation (1.13), that for any  $\Delta > 0$ , as long as  $\mu = 0$ , the edge Majoranas states  $\gamma_{A,0}$  and  $\gamma_{B,N-1}$  appear as zero energy modes. Thus Figure A, in Figures 1.8, depicts a topological phase. This was also already proved by the numerical diagonalization of the Hamiltonian in Figure 1.7.

What happens to the zero energy modes if we increase the chemical potential  $\mu$ ? Recall that the Hamiltonian 1.5 is particle-hole symmetric, thus the spectrum has to be symmetric around zero energy, see (1.10). When  $\mu = 0$ , two zero energy modes appear, corresponding to the Majorana modes which are localized far away from

each other. Trying to move these levels from zero energy individually is impossible, as it would violate particle-hole symmetry. By increasing the chemical potential, the energy gap remains present and particle-hole symmetry must remain satisfied, thus the zero energy modes must persist. The only possibility to move the energy modes from zero is to couple the two unpaired Majorana modes to each other. However, because of the spatial separation between Majoranas and of the presence of an energy gap, this coupling is impossible. The only way to couple the Majorana modes in energy is to close the bulk energy gap, which happens for  $\mu = 2t$ , see Figure E.

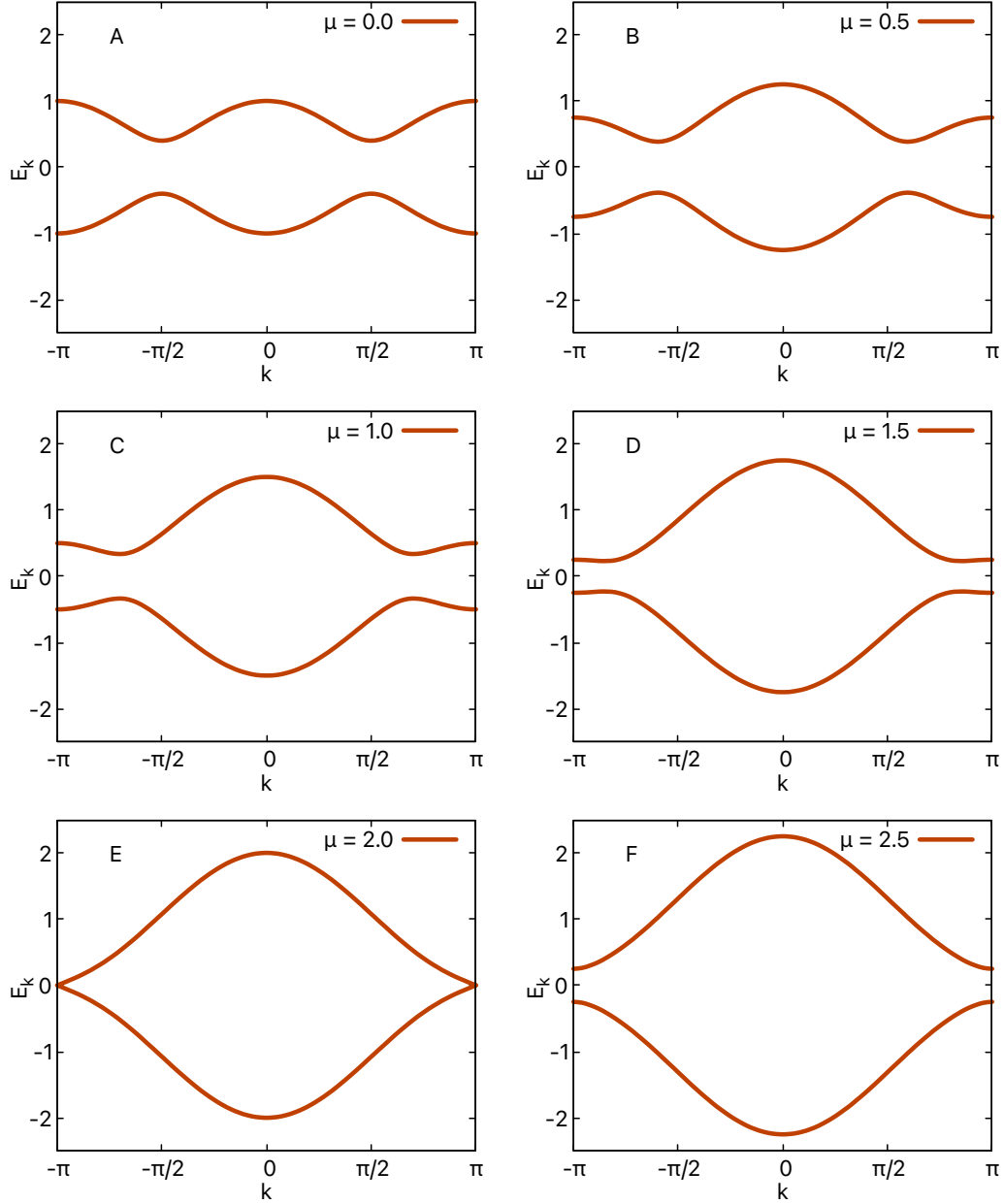


**Figure 1.8.** The energy spectrum in momentum space, given by equation (1.25), considers  $k$  as a continuous variable within the Brillouin Zone. For this spectrum, with parameters  $\Delta = 0.4t$ ,  $t = 1$  and  $a = 1$ , observe in Figure E how the energy gap closes at  $\mu = 2t$ .

This means that there exists a smooth path from a Hamiltonian with  $\mu = 0$  to a Hamiltonian with  $\mu = 2t$  that preserves the topological criterion. Consequently, Figures A, B, C, and D all host zero mode MFs, protected by symmetry and the energy gap in the spectrum. These considerations lead to a compact condition: The topological criterion of the Kitaev model is satisfied as long as  $|\mu| < 2t$ . The modulus is present due the Hamiltonian being particle-hole symmetric.

We can obtain the square modulus of the wave function associated to the MFs using the transformation operators in equation (1.2) after identifying the zero-mode eigenvalues. These Majorana states are plotted, for different values of  $\mu$  in Figures 1.9, where the red curve represents the unpaired MF localized at site  $(A, 0)$ , while the blue curve is the the other unpaired MF localized at site  $(B, N - 1)$  as expected.

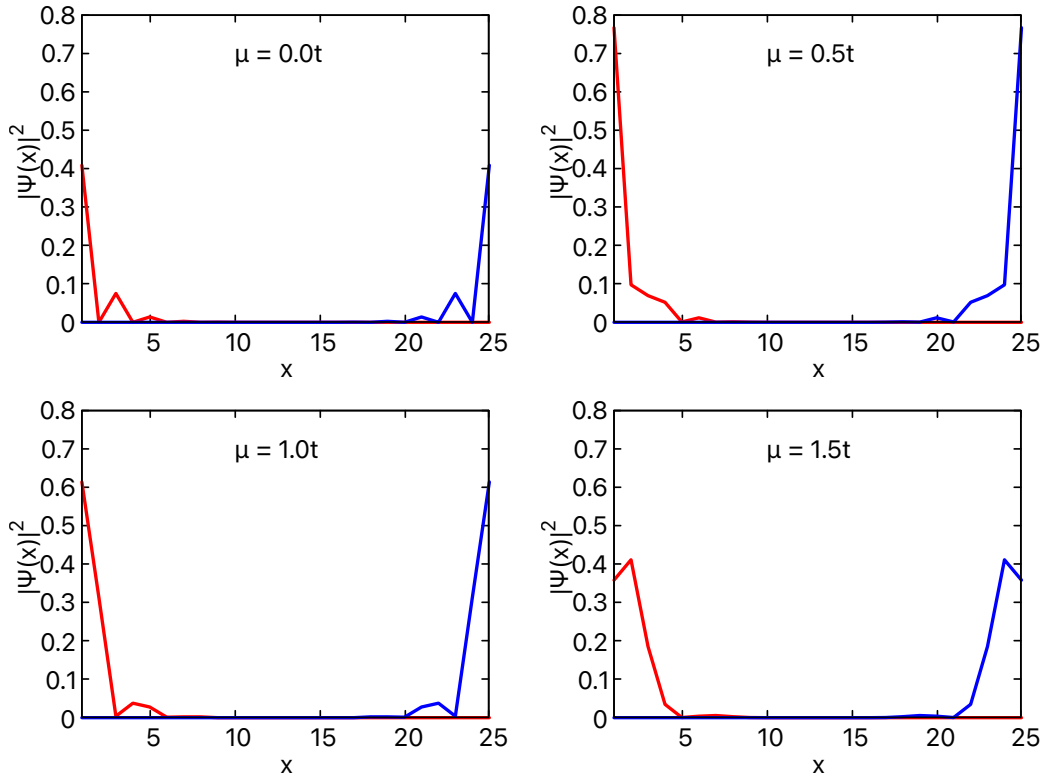


**Figure 1.9.** The localized Majorana zero energy modes for varying  $\mu$  at fixed  $\Delta = 0.4t$ ,  $t = 1$  and  $N = 25$ . The figure shows the square amplitude of the wave functions. The red curve represents the  $\gamma_A$  MF, meanwhile the blue curve represents the  $\gamma_B$  MF.

In the following section, we aim to demonstrate that MFs can be found in locations other than the edges of the chain, irrespective of whether the boundary conditions are open or closed.

## 1.4 Majorana modes appearing at a domain wall between different phases

Zero mode Majoranas are not only found at the edges of chains with open boundary conditions. They can also be located in other areas that do not depend on whether the boundary conditions are periodic or open.

To see this effect, we will firstly study the transition between the non-topological phase to the topological phase in momentum space with an effective Dirac model of the Kitaev Toy model. We focus on the gap closing at  $\mu = -2t$ , which happens at  $k = 0$ . Around the region where the two bands touch, we can make a linear expansion in  $k$  of the Hamiltonian (1.24) which, after neglecting  $o(k^2)$ , yields:

$$H(k) \simeq \begin{pmatrix} m & i\Delta k \\ -i\Delta k & -m \end{pmatrix} \quad (1.26)$$

Where we have defined  $m = -t - \mu/2$ . This effective Dirac Hamiltonian gives an energy spectrum  $E_k = \pm\sqrt{m^2 + \Delta^2 k^2}$  which is a good approximation of the exact band structure in (1.25) around  $\mu = -2t$ . The parameter  $m$  appearing in this Dirac Hamiltonian plays a crucial role in the understanding of the system. Its sign reminds us of the two phases which we encountered in the Kitaev Toy Model:

1. for  $m < 0$  (or  $\mu > -2t$ ) the system resided in the topological phase
2. for  $m > 0$  (or  $\mu < -2t$ ) the system resided in the non-topological phase

Let us consider the following problem: What happens if the parameter  $m(x)$  varies continuously in space, and changes sign at a certain point?

To answer this question we transform the effective Dirac Hamiltonian (1.26) back into real space:

$$H(x) = \begin{pmatrix} m(x) & \Delta\partial_x \\ -\Delta\partial_x & -m(x) \end{pmatrix} \quad (1.27)$$

We want the mass function  $m(x)$  to have the following property:

$$m(x) \xrightarrow{x \rightarrow \pm\infty} \pm m \quad (1.28)$$

And the point  $x = 0$  is the domain wall where the mass changes sign. By requiring  $\Psi$  to be a wave function that fulfills  $H\Psi = 0$ , representing our zero-mode MF, we derive an un-normalized solution:

$$\Psi(x) = \exp\left(-\text{sign}(m(x)) \int_0^x \frac{|m(x')|}{\Delta} dx'\right) \begin{pmatrix} 1 \\ \pm 1 \end{pmatrix} \quad (1.29)$$

In this final expression, we need to select  $\Psi$  in a way that ensures its normalizability. This solution gives a wave function localized at  $x = 0$ , with two exponential tails extending from either side. This constitutes our Majorana zero mode, see Figure 1.10:

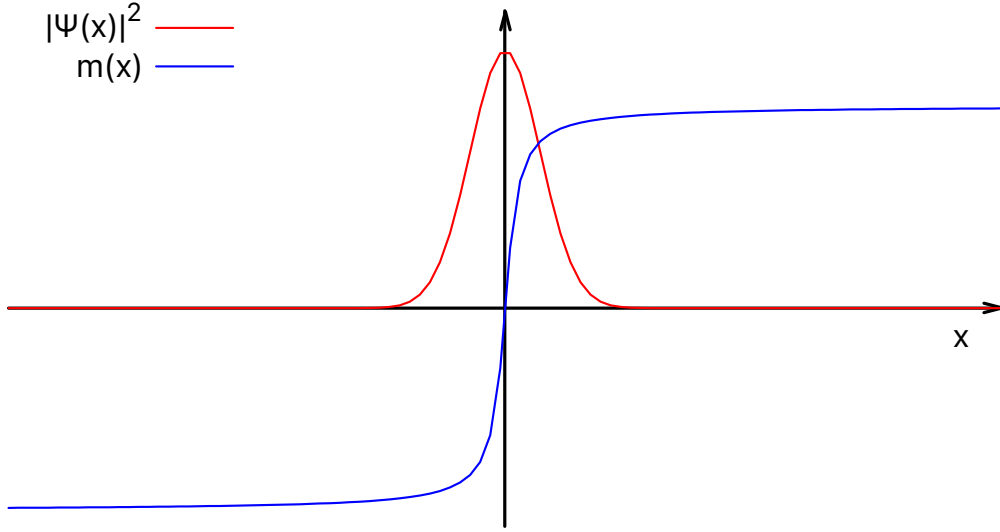


**Figure 1.10.** Schematic view of the zero energy Majorana mode localized at  $x = 0$  between the interface of a topological phase (for  $x < 0$ ) and the non-topological phase (for  $x > 0$ ). The mass  $m(x)$  is represented by the blue line; The modulus squared of the wavefunction  $|\Psi(x)|^2$  from equation (1.29) is represented by the red line.

It's important to highlight that without a sign change in  $m(x)$ , no zero mode would emerge, as  $\Psi$  wouldn't be normalizable on either side of the domain wall. From a physical perspective, we have demonstrated that in a system where the region is topological for  $x < 0$  and non-topological for  $x > 0$ , there must be a zero-mode MF at the interface between these two regions. This means that when two different pairing configurations are combined, a single unpaired MF must be left at the junction where they meet, see figure 1.11.

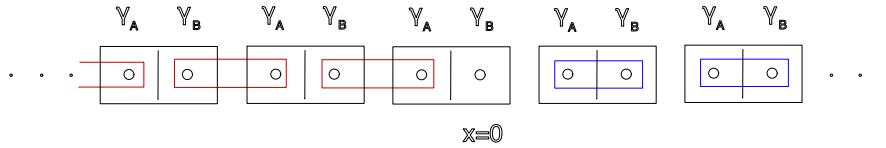


**Figure 1.11.** Illustration of an unpaired MF at the interface between a topological phase and a trivial phase.

## Chapter 2

# Coupling The Kitaev Model to a Classical Elastic Field at Half Filling

In the pursuit of understanding topological superconductors, numerous theoretical physicists have explored variations and extensions of the Kitaev Toy model, modifying its framework to investigate new phenomena. In this chapter, we take a similar approach: we introduce a classical elastic field coupled to the electrons within the system. By introducing this elastic field into the system, we want to unravel the new dynamics it brings to the topological phase. This field will play a crucial role in generating interfaces within the system, which, as we will demonstrate, will localize Majorana fermions.

We will focus specifically on examining the model at half filling, which corresponds to  $\mu = 0$  in the Kitaev model. This choice is particularly significant because it continues from where Kitaev left off, and it will reveal the emergence of a new phase upon introducing the electron-field coupling. This analysis will serve as a foundational exploration before we extend our investigations to the general case in a later chapter involving different electron densities in the system.

### 2.1 The Hamiltonian

The Hamiltonian that we will examine encompasses all the components of the original Kitaev toy model, as outlined in equation (1.5), augmented by the incorporation of the interaction of the electron density with a classical elastic field:

$$\begin{aligned}
 H = & -t \sum_{l=0}^{N-1} (c_l^\dagger c_{l+1} + c_{l+1}^\dagger c_l) + \Delta \sum_{l=0}^{N-1} (c_l^\dagger c_{l+1}^\dagger + c_{l+1} c_l) - \mu \sum_{l=0}^{N-1} c_l^\dagger c_l + \\
 & + \sum_{l=0}^{N-1} g X_l c_l^\dagger c_l + \sum_{l=0}^{N-1} \frac{1}{2} K X_l^2
 \end{aligned} \tag{2.1}$$

In this Hamiltonian we introduce  $X_l$  as the field variable at site  $l$ . Here,  $g > 0$  and  $K > 0$  serve as coupling constants. The term  $g X_l c_l^\dagger c_l$  denotes a linear association between electron density at each site and the field variable, where  $g$  quantifies the strength of this coupling. Additionally,  $\frac{1}{2} K X_l^2$  represents a harmonic (elastic) potential for the field, with  $K$  determining the stiffness of this potential.

The Hamiltonian (2.1) shares similarities with a model introduced by Theodore Holstein in 1959, which describes the interaction between electrons and phonons in a crystalline solid [29]. Interpreting the electron-field term in our model as an electron-phonon interaction, two main differences arise. First, unlike Holstein's model, our Hamiltonian includes an additional superconducting term  $\Delta \sum_l (c_l^\dagger c_{l+1}^\dagger + c_{l+1} c_l)$  and lacks the free oscillating phonon term  $H_{ph} = \hbar\omega_0 \sum_l b_l^\dagger b_l$ , where  $b_l^\dagger$  and  $b_l$  are the standard creation and annihilation operators, and  $\omega_0$  is the phonon frequency. Second, our Hamiltonian would characterize the interpretation of the field as phonons through a classical displacement field  $X_l$ , representing the average displacement of atoms from their equilibrium positions, rather than quantizing the phonon energy. While Holstein's model provides a more detailed description, we simplify the treatment by using a classical elastic field, replacing the full phonon energy term  $H_{ph}$  (which would include both kinetic and potential energy terms) with just the classical potential energy term. Thus, our model serves as a simplified version. However, readers interested in a more comprehensive description of the electron-phonon interaction may refer to Holstein's model.

Having introduced the Kitaev model with electron-field interactions we will see in the following discussion which configurations of  $X_l$  are interesting to explore that will give rise to different topological or non-topological phases.

### 2.1.1 Emerging New Phase

Identifying different configurations of  $X_l$  for the system will lead to different phases, hopefully topological phases with the presence of zero mode MFs. Examining the most straightforward scenario where the lattice displacement is a constant at every site  $l$ , that is  $X_l = X_0$ , we observe that the Hamiltonian can be understood as the original Kitaev Hamiltonian, though with an additional shift in the energy ground state by  $\frac{1}{2}KNX_0^2$ , alongside a transformation where the chemical potential is adjusted by a constant factor:

$$\mu \rightarrow \tilde{\mu} = \mu - gX_0 \quad (2.2)$$

The Hamiltonian (2.1) with  $X_l = X_0$  is then:

$$\begin{aligned} H = & -t \sum_{l=0}^{N-1} (c_l^\dagger c_{l+1} + c_{l+1}^\dagger c_l) + \Delta \sum_{l=0}^{N-1} (c_l^\dagger c_{l+1}^\dagger + c_{l+1} c_l) + \\ & -\tilde{\mu} \sum_{l=0}^{N-1} c_l^\dagger c_l + \frac{1}{2}KNX_0^2 \end{aligned} \quad (2.3)$$

In the original Kitaev model, the system reached half filling when  $\mu$  equaled zero. However, in this modified version incorporating electron-field interactions, setting the chemical potential to zero doesn't necessarily indicate the system is halfway occupied. Hence, introducing the new *symmetric chemical potential*  $\tilde{\mu}$  is necessary to achieve particle-hole symmetry. Therefore setting  $\tilde{\mu} = 0$ , the condition of half filling is met (One can prove this by studying the particle-hole symmetry).

This condition of half filling presents an interesting scenario due to the occurrence of an instability - this instability arises from a specific alignment between the Fermi surface and a wave vector that is in resonance with the periodicity of the crystal lattice. This periodicity can also be seen in the energy spectrum in reciprocal space in Figure 1.8: the periodicity of the Brillouin zone for  $\mu = 0$  is  $\pi$ , unlike all the other cases for  $\mu > 0$  where it is  $2\pi$ . This alignment, known as nesting (to see



more check [30]), enhances the interactions between electrons within the material. As a consequence, it can lead to significant changes in the material's properties, potentially giving rise to phenomena such as the formation of charge density waves (CDWs), ergo a new phase. Indeed, due to the linear coupling between the elastic deformation  $X_l$  and the electron density, a modulation of the former is accompanied by a corresponding modulation of the latter.

For this reason, it becomes inviting to explore solutions at half filling of  $X_l$  that may give rise to a CDW. Hence, we seek solutions of the form of the simplest CDW:

$$X_l = X_0 + (-1)^l X \quad (2.4)$$

Here  $X$  is the dimerization order parameter. It denotes the CDW, i.e., the new phase exhibited by the system, hereby after referred to as the dimerized phase, corresponding to an alternating value of the elastic deformation and of the electron density. Meanwhile the other phase  $X_0$  will be referred as the homogeneous phase. To see under what circumstances does the system, at half filling and  $T \rightarrow 0K$ , favor transitioning into the dimerized phase as opposed to the homogeneous phase we have to construct a phase diagram.

## 2.2 Phase Diagram at Half Filling

To construct a phase diagram, our initial focus lies in examining the system's Helmholtz free energy and minimizing it. This involves exploring the spectrum of energy in the system. To do so, we continue from the discussion in section (2.1), where we reason why an interesting solution of  $X_l$  is (2.4) which, when substituted into the Hamiltonian (2.1), at half filling results in:

$$\begin{aligned} H = & -t \sum_{l=0}^{N-1} (c_l^\dagger c_{l+1} + c_{l+1}^\dagger c_l) + \Delta \sum_{l=0}^{N-1} (c_l^\dagger c_{l+1}^\dagger + c_{l+1} c_l) + \\ & + gX \sum_{l=0}^{N-1} (-1)^l c_l^\dagger c_l + \frac{1}{2} K N X^2 \end{aligned} \quad (2.5)$$

In this final expression, we neglected the additional term  $\frac{1}{2} K N X_0^2$  which serves as a constant offset to the energy, which remains fixed and can be therefore disregarded. It can be disregarded because, if we want to meet the condition of half-filling, i.e.,  $\tilde{\mu} = 0$ , then  $X_0$  must be fixed in equation (2.2). With the introduction of this new dimerized phase  $X_l = (-1)^l X$ , we ask ourselves whether this possible emerging phase maintains the symmetries of the original Kitaev model? The answer is no.

### 2.2.1 Breaking of the Particle-Hole Symmetry

Let's revisit the concept of particle-hole symmetry, distinct from its previous discussion in Section (1.3): We define it as an antiunitary operator  $C$ , that satisfies  $CHC^{-1} = H$ , where  $H$  is a particle-hole symmetric Hamiltonian, see more in [31]. This operator can be introduced through the following mapping:

$$\begin{cases} C c_l C^{-1} = (-1)^l c_l^\dagger \\ C c_l^\dagger C^{-1} = (-1)^l c_l \end{cases} \quad (2.6)$$

Lets consider the linear term in  $X$  from the Hamiltonian (2.5) and see if it satisfies particle-hole symmetry:

$$C \left( gX \sum_{l=0}^{N-1} (-1)^l c_l^\dagger c_l \right) C^{-1} = - \left( gX \sum_{l=0}^{N-1} (-1)^l c_l^\dagger c_l \right) \neq \left( gX \sum_{l=0}^{N-1} (-1)^l c_l^\dagger c_l \right) \quad (2.7)$$

Therefore, the existence of the dimerized phase, if formed, inevitably breaks the particle-hole symmetry in the Hamiltonian (2.1). What remains preserved is the combination of parity and particle-hole symmetry. This breaking of symmetry suggests, according to principles of topology: where symmetries are broken, distinct topological phases may emerge. We can see more on this symmetry breaking in different results like the energy spectrum, but since the spectrum of the Hamiltonian (2.5) cannot be solved analytically in real space, we attempt to transform the Hamiltonian into the Bogoljubov-de Gennes form in momentum space using the same approach as described in section 1.3.3.

### 2.2.2 Description of the System in Reciprocal Space

Transitioning to reciprocal space, or momentum space, presents a subtle yet crucial distinction, underscoring the significance of the dimerized phase. Consider the Fourier transformation of the following term from the Hamiltonian (2.5) (check Appendix A for detailed calculations):

$$gX \sum_{l=0}^{N-1} (-1)^l c_l^\dagger c_l = gX \sum_k c_k^\dagger c_{k+\frac{\pi}{a}} \quad (2.8)$$

It is impossible to write this term in the Bogoljubov-de Gennes form using the same Nambu vector  $\Psi_k^\dagger = (c_k^\dagger \ c_{-k})$  as we did in (1.24) in the original Kitaev toy model. Therefore the presence of a dimerized phase forces us to introduce a new Nambu vector of a higher dimension:

$$\Psi_k^\dagger = \left( c_k^\dagger \ c_{k+\frac{\pi}{a}}^\dagger \ c_{-k} \ c_{-k-\frac{\pi}{a}} \right) \quad (2.9)$$

Using this new Nambu vector (2.9) the Hamiltonian (2.5) can be written in the Bogoljubov-de Gennes form:

$$H = \sum_{k \in D} \Psi_k^\dagger \begin{pmatrix} \xi_k & \frac{gX}{2} & -i\Delta_k & 0 \\ \frac{gX}{2} & \xi_{k+\frac{\pi}{a}} & 0 & -i\Delta_{k+\frac{\pi}{a}} \\ i\Delta_k & 0 & -\xi_k & -\frac{gX}{2} \\ 0 & i\Delta_{k+\frac{\pi}{a}} & -\frac{gX}{2} & -\xi_{k+\frac{\pi}{a}} \end{pmatrix} \Psi_k + \frac{1}{2} N K X^2 \quad (2.10)$$

Yielding the spectrum:

$$E_k^{\eta,\nu} = \eta \sqrt{\xi_k^2 + (\Delta_k + \nu \frac{gX}{2})^2} \ , \eta = \pm 1 \ , \nu = \pm 1 \quad (2.11)$$

Where we use definitions for  $\xi_k = -t \cos(ka)$  and  $\Delta_k = \Delta \sin(ka)$ . The domain  $D$  of the momentum space variable  $k$  holds greater significance in this context: Here it is defined as  $D = (0, \frac{2\pi}{Na}, \dots, \frac{2\pi}{Na} \cdot (\frac{N}{2} - 2), \frac{2\pi}{Na} \cdot (\frac{N}{2} - 1))$ .

In the absence of the electron-field interaction, specifically in the Kitaev toy model, the Bogoliubov-de Gennes Hamiltonian manifested as a  $2 \times 2$  dimensional

matrix. It yielded two eigenvalues corresponding to energies equivalent in modulus but opposite in sign, for each of the  $N$  distinct  $k$  values. This signifies a total energy spectrum of  $2N$  values. In the scenario of dimerization, the Hamiltonian matrix expands to a  $4 \times 4$  dimension, thereby producing four eigenvalues. However, the number of modes has reduced to half,  $N/2$ . This conservation maintains the number of degrees of freedom, indicating that the total energy spectrum remains  $4 \cdot N/2 = 2N$ . Another interesting interpretation arises when pairing each even site  $l$  with the subsequent site  $l + 1$ , treating them as a composite particle with a new lattice point in between. Consequently, this arrangement doubles the spacing between these composite particles to  $2a$ . As a result, the length of the chain remains constant, but the number of particles has halved to  $N/2$ , see Figure 2.1: This, in

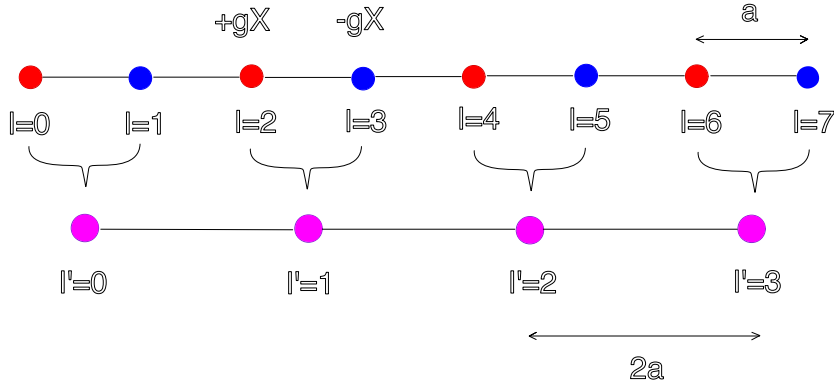


**Figure 2.1.** Illustration of dimerization symmetry for  $N = 8$ : even sites (red circles) have higher charge density due to an additional term  $+gX$  in the chemical potential, while odd sites (blue circles) have lower charge density due to a subtractive term  $-gX$ . Treating them as composite particles (pink circles) doubles the spacing and halves the number of lattice points to  $N' = 4$ .

turn, effectively halves the Brillouin zone. This halving of the Brillouin zone can also be seen by the spectrum in momentum space from equation (2.11), see Figures 2.2:

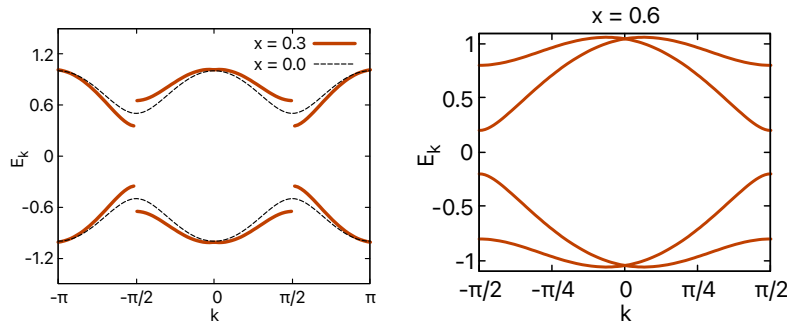


**Figure 2.2.** The halving of the Brillouin Zone at half filling due the presence of a dimerized phase. Here,  $E_k$  is the energy spectrum in momentum space,  $x = gX$ ,  $\Delta = 0.5t$ ,  $t = 1$  and  $a = 1$ ; The left figure illustrates how the presence of the dimerized phase breaks the continuity of the spectrum, depicted by red lines for  $x = 0.3$ , at  $k = \pm\pi/2$ . The energy spectrum without the dimerization, i.e.,  $x = 0$ , is shown by the black dashed line. Meanwhile, the right figure offers the energy spectrum for  $x = 0.6$  in momentum space from equation (2.11), we see indeed that the Brillouin Zone is halved.

In statistical mechanics, the main powerful tool to understand the behavior of phases is the Helmholtz free energy  $F$  [32] [33], it is defined as:

$$F = \Omega + \mu \cdot N_e \quad (2.12)$$

Where  $\Omega$  is the grand canonical potential and  $N_e$  the number of particles. By examining different parameters of the Hamiltonian, we can unveil the system's inclination towards particular phases. Simply put, where the free energy reaches its lowest point between all the possible phases, that's where the system prefers to be. Equipped with the analytical expression for the system's spectrum (2.11), we can determine whether the system leans towards a dimerized or homogeneous phase by examining the global minima of the Helmholtz free energy.

At half filling, the Helmholtz free energy coincides with the grand canonical potential. One can prove this by simply expressing the free energy in terms of  $\tilde{\mu}$  instead of  $\mu$  and recall that half filling is met when  $\tilde{\mu} = 0$ . Consequently, studying the Helmholtz free energy simplifies to studying the grand canonical potential per lattice site  $\omega$ , given by:

$$\omega = -\frac{1}{\beta N} \sum_{\eta=\pm 1} \sum_{\nu=\pm 1} \sum_{k \in D} \log(1 + e^{-\beta E_k^{\eta,\nu}}) + \frac{1}{2} K X^2 \quad (2.13)$$

Which for temperatures going to absolute zero, that is  $\beta \rightarrow +\infty$ , gives:

$$\omega = -\frac{1}{N} \sum_{k \in D} \sqrt{\xi_k^2 + \left(\Delta_k + \frac{gX}{2}\right)^2} + \sqrt{\xi_k^2 + \left(\Delta_k - \frac{gX}{2}\right)^2} + \frac{1}{2} K X^2 \quad (2.14)$$

In this last equation (2.14) the grand canonical potential per lattice site is a function of different variables, i.e.,  $\omega = \omega(t, \Delta, g, K, X)$ . We can define new variables:

$$\begin{cases} \lambda = g^2/K \\ x = gX \end{cases} \quad (2.15)$$

Since the hopping parameters is always  $t \neq 0$ , we can express all the other variables of the grand canonical potential in units of  $t$ . This transforms:

$$\omega(t, \Delta, g, K, X) \rightarrow \omega(\Delta, \lambda, x) \quad (2.16)$$

With this last transformation, everything becomes dimensionless. The new variable  $\lambda$  quantifies the strength of the coupling. It is noteworthy that  $\lambda = 0 \iff g = 0$ .

Given  $\lambda$  and  $\Delta$ , the dimerized phase emerges solely when its Helmholtz free energy is less than that of the homogeneous phase configuration, this translates to searching solutions for  $x$  that satisfy:

$$\omega(\Delta, \lambda, x) < \omega(\Delta, \lambda, 0) \quad (2.17)$$

Since equation (2.17) is defined over a three-dimensional space, we can firstly fix  $\lambda$  and then slowly vary  $\Delta$  and study the behavior of  $\omega$  as a function of  $x$ . Doing so we see that there exists a  $\Delta$  critical, defined as  $\Delta_c$ , below which the the system would prefer to construct a dimerized phase, see Figures 2.3.

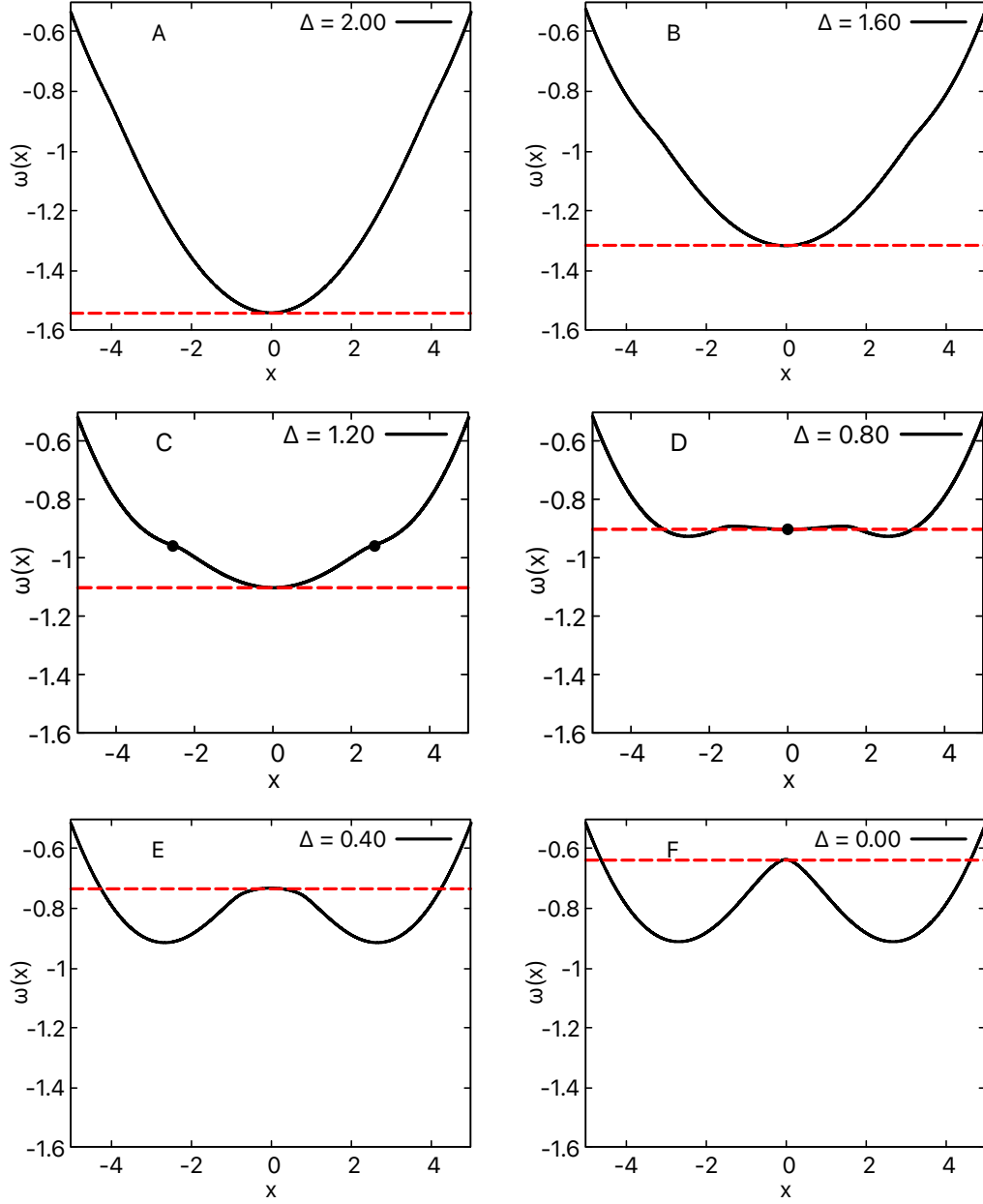


**Figure 2.3.** The grand canonical potential per lattice site  $\omega(x)$  (black line), which is equal to the Free Helmholtz Energy at half filling, and they all depend on multiple variables, for different values of  $\Delta$ ; here,  $t = 1$ ,  $x = gX$ ,  $\lambda = 6.00$  and  $N = 400$ . The dashed red line represents the energy configuration of the homogeneous phase, that is  $\omega(0)$ . If the black line is below the red line, the system prefers to construct a dimerized CDW. For the cases A,B and C:  $\Delta > \Delta_c$  and the system prefers to create a homogeneous phase, meanwhile for the cases of D,E and F:  $\Delta < \Delta_c$  and the system constructs the dimerized phase. Figure C shows the formation of a local minima for  $x > 0$ , indicating a spinodal points of the dimerized phase (black dots). Conversely, Figure D shows a local minima at  $x = 0$ , corresponding to the spinodal point of the homogeneous phase (also marked by a black dot).

### 2.2.3 The phase transition

Figures 2.3 motivate us to further study analytically and numerically  $\omega$  to construct a phase diagram: We can look for the equilibrium condition  $\partial_X \omega = 0$  that yields the self-consistency equation:

$$X = \frac{g}{2NK} \sum_{k \in D} \left[ \frac{\frac{gX}{2} + \Delta_k}{\sqrt{(\frac{gX}{2} + \Delta_k)^2 + \xi_k^2}} + \frac{\frac{gX}{2} - \Delta_k}{\sqrt{(\frac{gX}{2} - \Delta_k)^2 + \xi_k^2}} \right] \quad (2.18)$$

The self-consistency equation (2.18) has always a solution  $X = 0$  corresponding to the homogeneous phase. As  $\lambda$  grows large, the solution becomes dimerized, with  $|X| = g/2K$ . At intermediate values of  $\lambda$ , a first-order transition takes place, transitioning between the dimerized phase and the homogeneous phase. This phase transition occurs when the Helmholtz free energy of the homogeneous phase becomes equal to free energy of the dimerized phase, that is when:

$$\omega(\Delta, \lambda, x) = \omega(\Delta, \lambda, 0) \quad (2.19)$$

We can also expand for small  $X$  the self-consistency equation (2.18) to obtain the limit where the homogeneous phase can exist as a local, but not overall, minima of the free energy. This expansion gives the equation:

$$1 = \frac{g^2}{2NK} \sum_{k \in D} \frac{\xi_k^2}{\sqrt{\Delta_k^2 + \xi_k^2}^3} \quad (2.20)$$

Having all this information about the system, we can construct the phase diagram at half filling between the dimerized and homogeneous phase, see Figure 2.4:

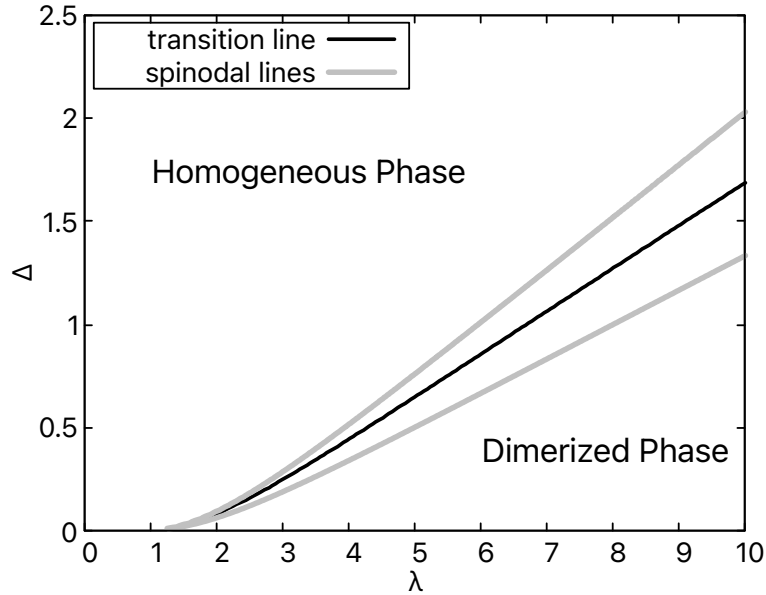


**Figure 2.4.** The phase diagram at half filling. The solid line is the first order phase transition line separating the dimerized non-topological phase (bellow the line) from the undimerized topological phase (above the line). The two gray lines are the loci of the spinodal points of the first order transition.

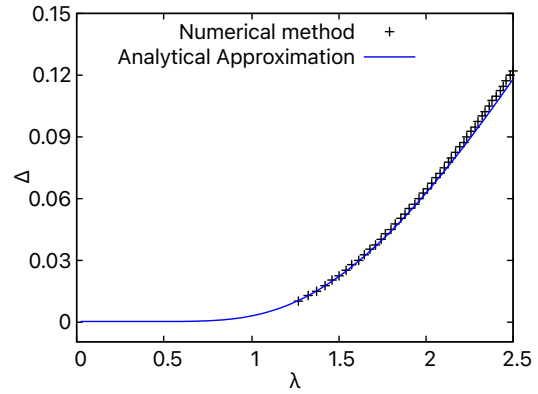
The solid line is the first order phase transition line separating the dimerized non-topological phase, which exists up to a certain  $\Delta_c(\lambda)$ , from the homogeneous topological phase. We know that this homogeneous phase is topological since it can be interpreted as the Kitaev toy-model in the absence of electron-field interactions. Since Kitaev demonstrated that for the parameters  $(\mu = 0, \Delta = t = 1)$ , which, in the presence of the electron-field interaction, correspond to  $(\tilde{\mu} = 0, \Delta = t = 1)$ , it follows that for any pair  $(\lambda', \Delta')$ , above the phase transition line, one can construct a smooth path connecting two different Hamiltonians  $H(\lambda = 0, \Delta = 1)$  and  $H(\lambda', \Delta')$ . This path must necessarily maintain the topological criterion of the initial Hamiltonian, specifically the presence of MFs. The phase diagram shows that after a certain  $\Delta_c(\lambda)$  dimerization is not possible anymore. The two gray lines are the loci of the spinodal points of the first-order transition.

In the vicinity of  $(\Delta, \lambda) \rightarrow (0^+, 0^+)$ , equations (2.18), (2.19), and (2.20) all present a common challenge. This arises from them containing sums that can be converted into elliptical integrals, which tend to diverge as  $\Delta \rightarrow 0^+$ . To address this issue, we approach  $\Delta$  as an infinitesimal parameter. Once the sums are transformed into integrals, we can analytically solve them around the regions where the integrals become divergent as  $\Delta \rightarrow 0^+$ . Let's consider the equation (2.20) that generates the bottom spinodal line in Figure 2.5. If we treat  $\Delta$  as an infinitesimal parameter, the spinodal line exhibits the following behavior:

$$(2.20) \rightarrow \Delta = \epsilon \sqrt{\frac{2}{3}} \frac{1}{\sqrt{e^{\frac{4\pi}{\lambda}} - A(\epsilon)} - 1} \propto e^{-\frac{2\pi}{\lambda}} \quad (2.21)$$

Where  $\epsilon$  is a finite positive parameter and  $A(\epsilon)$  is a polynomial. To see the definition of  $A(\epsilon)$  and the treatment of this divergence, check Appendix B. The behavior of the bottom spinodal line for the region corresponding to small  $\Delta$  can be observed in Figure 2.5. By mathematical construction the phase transition line and the top spinodal contain the same divergencies inherited from elliptic functions thus have a similar approximation for  $\Delta \ll 1$ .

**Figure 2.5.** The bottom spinodal line at half filling for small  $\Delta$ . Here  $\epsilon = 0.95$ . The blue line represents the analytical approximation for small  $\Delta$  given in equation (2.21) meanwhile the black points represent the numerical computation of equation (2.18).



## 2.3 The Zero Modes Persist

The results from Section 1.3 are also evident in the presence of electron-field interactions. With this interaction at half filling, the system constructs a topological phase, but only when  $\Delta$ , dependent upon  $\lambda$ , is sufficiently large. This last condition negates the emergence of a dimerized non-topological phase.

We can prove the difference of the topological phases also by looking at the energy spectrum in real space by performing a numerical diagonalization of the Hamiltonian (2.5) for fixed  $\Delta$  and different values of  $\lambda$ , see Figure 2.6:

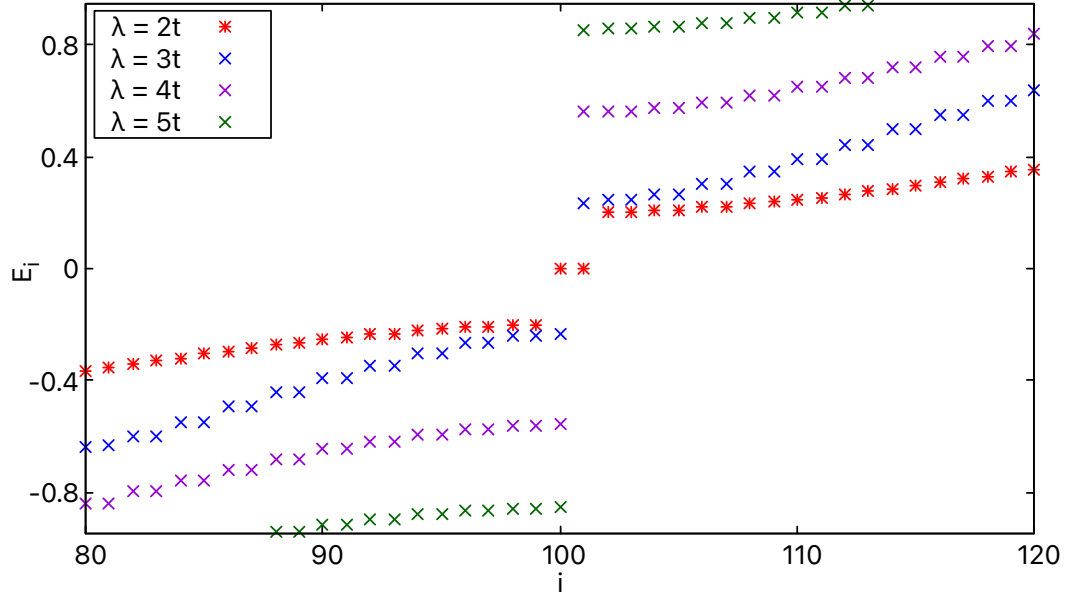


**Figure 2.6.** The energy spectrum at the global minima of the free energy and half filling for  $\lambda \in (2t, 3t, 4t, 5t)$  is given under the conditions  $\Delta = 0.2t$ ,  $t = 1$ , and  $N = 100$ . Here,  $i = 0, 1, \dots, 2N - 1$  labels the energy levels in increasing order. For  $\Delta = 0.2t$ , the critical value of  $\lambda$  is  $\lambda_c = 2.79t$ , indicating a phase transition in the system. For any  $\lambda < \lambda_c$ , the topological criterion is met, always yielding the same energy spectrum featuring a doubly-degenerate zero-mode. Conversely, for  $\lambda > \lambda_c$ , the system transitions to a non-topological dimerized phase, without zero modes.

The phase diagram, Figure 2.4, reveals a competition within the system between a phase generating a non-topological CDW and a topological homogeneous phase. It is well known that CDWs are destabilized away from the half filling condition [34]. On the other hand moving away from half filling will ultimately lead to a non topological phase as far as the topological condition is not fulfilled. It is therefore interesting to study the system outside of half filling where it could tend towards a CDW resembling the dimerized non-topological phase, or perhaps transitions into a different phase capable of accommodating MFs. To understand this problem, the following chapter examines the system's electronic susceptibility, which will establish the conditions for the formation of CDWs, other phases and the system's topological criterion.



## Chapter 3

# The Model Away from Half Filling

In the previous chapter, we examined at half filling the coupling of the Kitaev Model to a classical elastic field, hereinafter referred to as CKM - The Coupled Kitaev Model. This study demonstrated that when the Kitaev model is coupled with a classical elastic field, given specific values of  $\Delta$  and the coupling constant  $\lambda$ , as defined in (2.15), lead to a first-order phase transition separating a topological phase from a non-topological dimerized phase, i.e., a CDW, see Figure 2.4. The primary aim of this thesis is not to investigate the formation of CDWs and other phases, but rather to gain a deeper understanding of CKM and to identify the regions where the phases become topological and can host zero-mode Majoranas, especially at varied electron densities. To determine these regions, we first need to understand the conditions under which the system prefers to form CDWs. One way to do this is by considering the classical elastic field as analogous to the classical phonon field. This allows us to draw a parallel to the Peierls instability in one-dimensional metals [35] and the formation of CDWs through the study of electronic susceptibility [36]. After identifying the regions where CDWs and other phases form, we can disregard those areas, as we expect them to be non-topological due to symmetry breaking, similar to that of the dimerized phase at half filling. Our focus will be on the remaining regions, which are of interest and are anticipated to be topological phases.

### 3.1 Peierls Instability and CDWs

Sir Rudolf Peierls, a physicist of German origin who later became a British citizen, formulated in 1930 what is now known as the Peierls theorem. It states that at low temperatures, a one-dimensional metal is unstable with respect to lattice distortions induced by even small external perturbations. Peierls specifically considered the case of a half-filled electronic band, where the Fermi wave vector  $k_F$  satisfies the condition  $2k_F = \pi/a$ , resulting in a commensurate lattice distortion with wave vector  $q = 2k_F$ . This periodic lattice distortion opens a gap at the Fermi level, thereby lowering the total electronic energy and stabilizing a new ground state - just like the energy gap formed at half filling from the dimerized phase, recall Figure 2.2. This phenomenon, known as the *Peierls instability*, leads to the formation of a CDW. While Peierls focused on the half-filled case, it is important to emphasize that the instability at  $q = 2k_F$  occurs at any filling, which we show in the following section for the Kitaev Model, due to the universal nesting property of the one-dimensional Fermi surface.

The formation of CDWs and Peierls instability can be understood by examining the electronic susceptibility of the system. When an external field characterized by a wavevector  $q$  affects the system, there exists a specific wavevector  $q = 2k_F$  where the susceptibility  $\chi(q)$  diverges. This divergence in  $\chi(q)$  indicates a strong tendency for the system to develop a CDW with the corresponding wavevector  $q = 2k_F$ . It is noteworthy to say that a divergence of  $\chi(q)$  does not always imply the formation of CDWs. Susceptibility can also diverge due to other reasons as we will see in the following analysis. However, it remains clear that the divergence of susceptibility indicates the presence of a phase transition in the vicinity. It is also notable to mention that since we are in a one-dimensional system, we are more prone to forming CDWs compared to higher-dimensional systems, see Figure 3.1. With this foundation laid, we can now go into the discussion of the Kitaev model's susceptibility to the formation of CDWs.

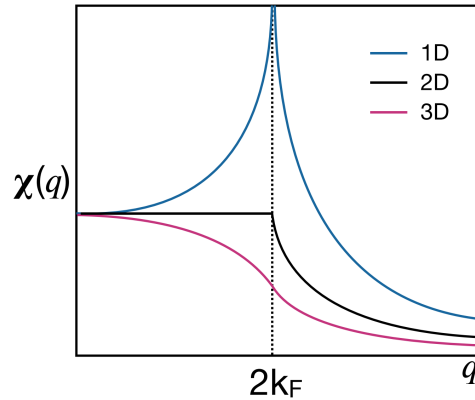


**Figure 3.1.** From [37], the electronic susceptibility in 1,2 and 3 dimensions. The divergence in one dimension is due the effect of the Peierls instability and the formation of CDWs.

#### 3.1.1 Susceptibility of the Kitaev Model

Susceptibility, in a broad thermodynamic context, refers to the extent to which a material responds to an external perturbation. Specifically, electronic susceptibility quantifies the response of the electron density within a system to changes in an

external field, such as an applied voltage or magnetic field. In our scenario, the external field affecting the electrons is the classical elastic field. This response is described by the electronic susceptibility function,  $\chi(q, T)$ , where  $q$  represents the wavevector of the classical elastic field, and  $T$  is the temperature. This function quantifies the system's ability to create regions with varying electron densities, aligned with the periodicity defined by the wavevector  $q$ . Peaks in  $\chi(q, T)$  indicate strong responses at specific wavevectors, suggesting potential instabilities that could lead to the formation of CDWs.

Let's consider the electronic susceptibility of the Kitaev model described in Section 1.3. This model is treated within the Nambu formalism, and we will maintain this approach to treat the susceptibility accordingly. For further details on this method, refer to [38]. Thus, the susceptibility is:

$$\chi(q, T) = -\frac{T}{\mathcal{V}} \sum_{k, \omega_n} \frac{1}{2} \text{Tr} [\hat{\mathcal{G}}(k - q/2) \sigma_z \hat{\mathcal{G}}(k + q/2) \sigma_z] \quad (3.1)$$

The fraction  $\frac{1}{2}$  in front of the trace is due to the fact that we are working with spinless fermions, unlike Nambu's formalism. Here,  $\mathcal{V}$  is the systems volume,  $k$  is the discrete momentum space variable with values  $k = (0, \frac{2\pi}{Na}, \dots, \frac{2\pi}{a} \frac{N-1}{N})$ ,  $T$  is the temperature,  $\hat{\mathcal{G}}$  is a  $2 \times 2$  matrix containing Green's Functions and  $\sigma_z$  is the third Pauli matrix. They are defined as:

$$\hat{\mathcal{G}}(k, \omega_n) = \begin{pmatrix} \mathcal{G}(k, \omega_n) & \mathcal{F}(k, \omega_n) \\ \mathcal{F}(k, \omega_n) & -\mathcal{G}(-k, -\omega_n) \end{pmatrix} \quad (3.2)$$

$$\sigma_z = \begin{pmatrix} 1 & 0 \\ 0 & -1 \end{pmatrix} \quad (3.3)$$

Where  $\omega_n$  are the Matsubara frequencies [39]. For fermions  $\omega_n = (2n + 1)\pi T$  and  $n \in \mathbb{Z}$ . The terms inside the matrix  $\hat{\mathcal{G}}$  are the Green's functions and the Anomalous Green's functions, given by:

$$\mathcal{G}(k, \omega_n) = \frac{-i\omega_n - \xi_k}{\omega_n^2 + E_k^2} \quad (3.4)$$

$$\mathcal{F}(k, \omega_n) = \frac{\Delta_k}{\omega_n^2 + E_k^2} \quad (3.5)$$

The energy  $E_k$  is defined as in (1.25). Solving the trace in equation (3.1) gives:

$$\chi(q) = -\frac{T}{\mathcal{V}} \sum_{k, \omega_n} \left[ \mathcal{G}(k - \frac{q}{2}, \omega_n) \mathcal{G}(k + \frac{q}{2}, \omega_n) - \mathcal{F}(k - \frac{q}{2}, \omega_n) \mathcal{F}(k + \frac{q}{2}, \omega_n) \right] \quad (3.6)$$

Inserting the expression for the Green's functions and taking the limit  $T \rightarrow 0K$  the susceptibility of the Kitaev model becomes:

$$\chi(q) = \frac{1}{2\mathcal{V}} \sum_k \frac{E_+ E_- - \xi_+ \xi_- + \Delta_+ \Delta_-}{E_+ E_- (E_+ + E_-)} \quad (3.7)$$

Where in this last equations the indices ' $\pm$ ' are defined as: Given a function  $g = g(k)$  which depends on the momentum space variable  $k$ , we define the functions  $g_{\pm}$  as  $g_{\pm} = g(k \pm q/2)$ . To see more on the derivation of equation (3.7) refer to Appendix C. Let's analyze what the susceptibility suggests for different values of  $\mu$  and  $\Delta$ , and identify the wavevector  $q$  at which  $\chi(q)$  diverges:

### The Kitaev susceptibility for $\Delta = 0$

For  $\Delta = 0$  it is possible to find the analytic expression of  $\chi(q)$ :

$$\chi(q) = \frac{1}{2\pi t a \sin \frac{q}{2}} \left| \frac{\tan(\frac{k_F}{2} + \frac{q}{4})}{\tan(\frac{k_F}{2} - \frac{q}{4})} \right| \quad (3.8)$$

And the Fermi wavevector is found by solving  $E(k_F) = 0$ , giving a solution:

$$k_F = \arccos\left(-\frac{\mu}{2t}\right) \quad (3.9)$$

The susceptibility is seen in Figure 3.2, we indeed see that there is a divergence at  $q = 2k_F$  and  $q = 2\pi - 2k_F$  for any value of  $|\mu| \leq 2t$  when  $\Delta = 0$ . This means that for  $\Delta = 0$  the system prefers to create CDWs. For  $|\mu| > 2t$  see the case susceptibility in general.

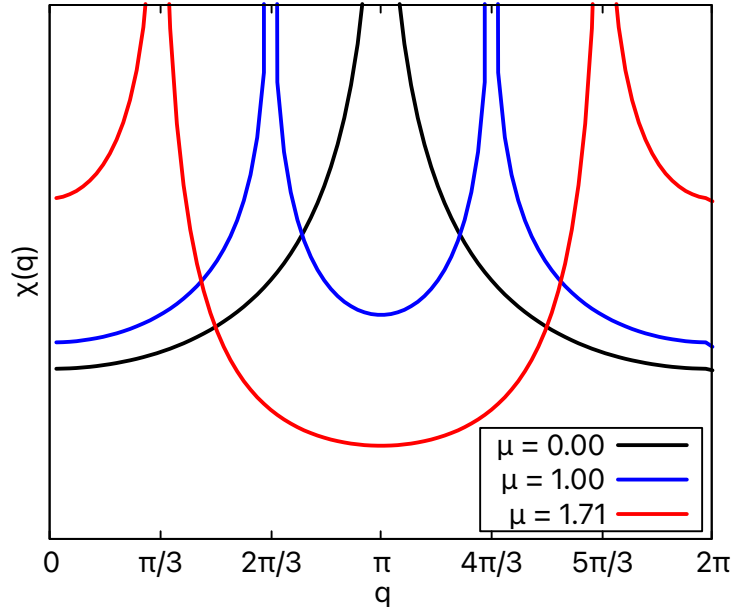


**Figure 3.2.** The Kitaev susceptibility for  $\Delta = 0$  and different values of  $\mu$ . For any value of  $|\mu| \leq 2t$  there is a divergence in the susceptibility suggesting a formation of a CDW.

### The Kitaev susceptibility for $\mu = 0$

For half filling, i.e.,  $\mu = 0$ , the susceptibility only diverges if  $\Delta = 0$ . As soon as the parameter  $\Delta > 0$  the susceptibility is non-divergent, see Figure 3.3. The Fermi wavevector is constant and it is  $k_F = \pi/2$ . We can prove that as  $\Delta \rightarrow 0$ , the susceptibility diverges. Indeed if we treat it as a small parameter we see:

$$\chi(\pi) \simeq \frac{2}{\pi a t} \log \left( 1 + \frac{2\epsilon^2}{3\Delta^2} \right) \xrightarrow{\Delta \rightarrow 0} +\infty \quad (3.10)$$

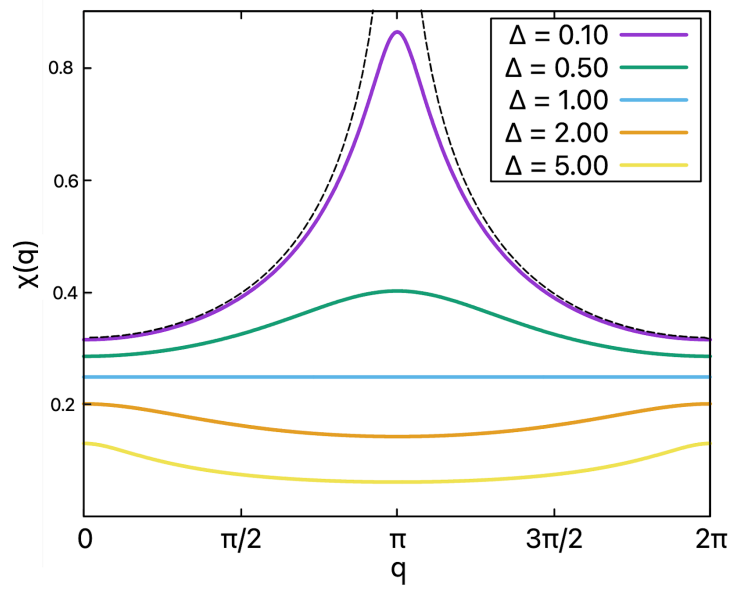


**Figure 3.3.** The Kitaev susceptibility for  $\mu = 0$  and different values of  $\Delta$ . The black dashed line represents  $\Delta = 0$ . This demonstrates that the presence of the superconducting parameter  $\Delta$  in the system conflicts with the formation of CDWs.

#### The Kitaev susceptibility for $|\mu| > 0$ and $\Delta > 0$

Lets consider firstly the Fermi wavevector  $k_F$  of the general spectrum in momentum space in equation (1.25). For a given general parameter  $\mu$  and  $\Delta$ , the Fermi wavevector is:

$$k_F = \arccos\left(-\frac{\mu}{2(1-\Delta^2)}\right) \quad (3.11)$$

Where in this last equation the hopping parameter is set to  $t = 1$ . Since the argument in the big parenthesis in this equation has to have a modulus smaller or equal to 1, this imposes a condition on what will be the wavevector  $q = 2k_F$  where the result of that wavevector gives an overall global maxima in the susceptibility. This wavevector can be characterized in the following manner:

$$q = \begin{cases} 2k_F & \text{if, } |\mu| \leq 2(1-\Delta^2) \\ 2\pi & \text{if, } |\mu| > 2(1-\Delta^2) \end{cases} \quad (3.12)$$

Another solution is always  $\tilde{q} = (2\pi - q)$ . For any pair  $\mu$  and  $\Delta > 0$ , the susceptibility does not exhibit any divergences, as illustrated in Figure 3.4. An exception arises where the susceptibility necessarily diverges not due to the system's tendency to form a CDW, but because it undergoes a phase transition from a topological phase to a non-topological phase. This transition point is known to be  $|\mu| = 2t$  in the Kitaev model. To study this further, we consider the region  $\mu = 2t(1 + \alpha)$  where  $\alpha$  is an infinitesimal parameter. This divergence occurs when  $q$  is a multiple of  $2\pi$ :

$$\chi(2\pi) = \frac{1}{\pi} \frac{\Delta^2}{\sqrt{\Delta^2 + \alpha^2}^3} \log\left(1 + \frac{2}{3} \frac{\Delta^2 + \alpha^2}{\alpha^2} \epsilon^2\right) \xrightarrow{\alpha \rightarrow 0} +\infty \quad (3.13)$$

Where  $\epsilon$  is a finite positive value.

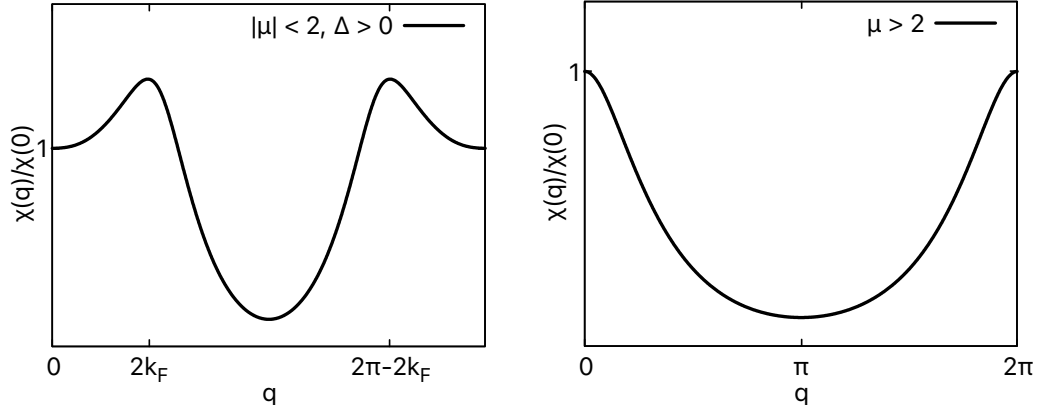


**Figure 3.4.** The Kitaev susceptibility for any  $\mu$  and  $\Delta > 0$ . Here  $t = 1$ . The figure on the left illustrates that for finite  $\Delta$  and  $|\mu| < 2t$ , there is no divergence. The figure on the right demonstrates that when  $|\mu| > 2t$ , regardless of the value of  $\Delta$ , no divergence occurs, and the susceptibility approaches zero as  $\mu$  increases.

In conclusion the susceptibility diverges, indicating it has a tendency to form CDWs, only for  $\Delta = 0$ . It diverges also when  $|\mu| = 2t$  but this divergence is not related to the formation of CDWs. This finding contradicts the phase diagram at half-filling, recall Figure 2.4, which clearly indicates the existence of a dimerized phase for values of  $\Delta > 0$ . This problem arises because the susceptibility given in (3.1) neglect the electron-electron interaction that arises via the coupling of the electron density to the classical elastic field. To compute the correct susceptibility we have to take a different approach.

### 3.1.2 Random Phase Approximation Approach

Given that the susceptibility of the Kitaev model inadequately describes the formation of the dimerized phase at half filling, as depicted in Figure 2.4, its validity for other cases where  $\mu \neq 0$  remains uncertain. Therefore, an alternative approach is necessary, and the Random Phase Approximation theory [40], hereinafter referred as RPA, emerges as the most suitable choice.

Let's analyze the susceptibility given in equation (3.6). We can interpret the expression as a bubble diagram  $\mathcal{B}_0(q)$ , which represents the difference between two distinct bubble diagrams: one composed of two regular Green's functions and another composed of two anomalous Green's functions, see Figure 3.5.

RPA theory explains that in the presence of an external field modulated by a wavevector  $q$ , the bubble diagram  $\mathcal{B}_0(q)$  represents the zeroth order in the terms of the coupling constant of the system with the external field. This corresponds to the scenario where no external field is present. In contrast, the real bubble diagram  $\mathcal{B}(q)$  includes an infinite series of higher-order bubble diagrams with increasing powers of the coupling constant. Refer to Figure 3.6.

Given that the coupling constant appearing in the RPA is  $2\lambda$ , which can be derived by examining the Peierls instability at half-filling, the real bubble diagram is:

$$\mathcal{B}(q) = \mathcal{B}_0(q) + \mathcal{B}_0(q)2\lambda\mathcal{B}_0(q) + \mathcal{B}_0(q)2\lambda\mathcal{B}_0(q)2\lambda\mathcal{B}_0(q) + \dots = \frac{\mathcal{B}_0(q)}{1 - 2\lambda\mathcal{B}_0(q)} \quad (3.14)$$

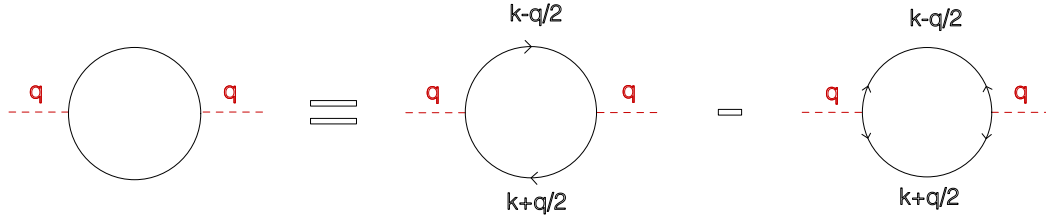


**Figure 3.5.** Representation of the bubble diagram  $\mathcal{B}_0(q)$ . This diagram consists of two components: one bubble diagram featuring two regular Green's functions, and another bubble diagram featuring two anomalous Green's functions, with the latter being subtracted from the former. In the diagram, the black lines denote the Green's functions, while the red line denote the external field.

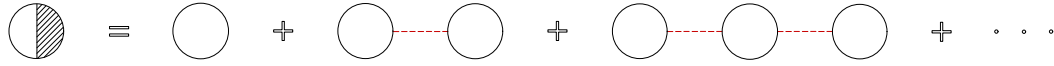


**Figure 3.6.** Representation of the real bubble diagram  $\mathcal{B}(q)$  at  $T = 0K$  from RPA theory. The empty bubbles represent the no-interaction bubble diagram  $\mathcal{B}_0(q)$  meanwhile the red dashed lines represent the coupling with the external field. RPA theory suggest that the real bubble diagram is an infinite sum of combinations of the no-interacting bubble diagram and the coupling with the Field.

Which translates equivalently to the susceptibility  $\chi(q)$  as:

$$\chi(q) = \frac{\chi_0(q)}{1 - 2\lambda\chi_0(q)} \quad (3.15)$$

Where  $\chi_0(q)$  would denote the Kitaev susceptibility without the electron-field interaction. The new evaluated susceptibility may diverge if the denominator in (3.15) is zero. This condition indicates that there is a divergence of the susceptibility if and only if:

$$1 - 2\lambda\chi_0(q) = 0 \quad (3.16)$$

Since  $\chi_0(q)$  is independent on  $\lambda$  the fulfillment of this equation establish a line  $\lambda(\mu, \Delta)$  in the phase diagram. This line cannot be directly linked to a phase transition because a first-order phase transition does not involve the divergence of a susceptibility.

Let's revisit the case of half filling, which has a Fermi wavevector  $k_F = \pi/2$ . When plotting  $\Delta$  versus  $\lambda(\chi(q = \pi, \mu = 0, \Delta))$ , we find that the resulting line is identical to the one obtained from equation (2.20). This line is the spinodal line, depicted as the gray line below the phase transition in Figure 2.4, which indicates the boundary below which a homogeneous phase cannot exist, not even as a local minimum in the free energy. This implies that, for values of  $\lambda$  bellow certain critical treshhold, equation (3.16) identifies the line below which CDWs and other phases occur, see Figure 3.7.

We point out that for every different  $\mu$ , in the plot  $\Delta$  versus  $\lambda$ , there is a discontinuity in the slope at a specific critical value of  $\lambda$ . This discontinuity can be understood by examining the half-filling case. The dashed dark-violet line represents the spinodal line of the homogeneous phase, considering only the formation of the dimerized and homogeneous phases. It is the boundary below which the homogeneous phase can no

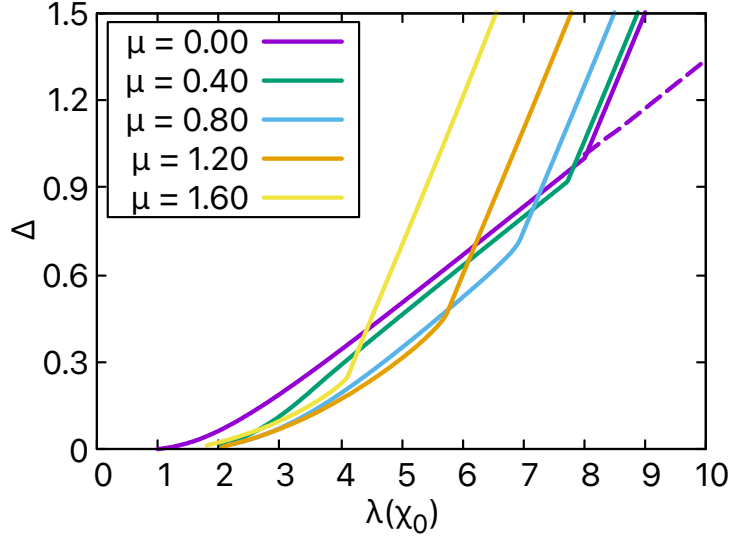


**Figure 3.7.**  $\Delta$  versus  $\lambda$  at different values of  $\mu$ . Here  $\lambda$  is a function of the susceptibility given by equation (3.16). The dark-purple line represents the case of half filling. The dashed purple line is the spinodal line of the homogeneous phase for  $\mu = 0$ , which is derived by considering only the formation of the dimerized and homogeneous phases. The regions below the full lines represent areas where other phases, additional to the CDWs, could emerge, which are not considered in this thesis and lie beyond its scope.

longer be formed. The change in slope, in Figure 3.7, at a critical  $\lambda$  arises because we did not account for other possible configurations of  $X_l$  that would enable the formation of different phases. Nevertheless, the region below each line remains valid, indicating the regions where the system begins to favor the formation of other phases rather than the homogeneous phase. Refer to Figure 3.8 for a different type of CDW, obtained computationally by minimizing the free energy under specific parameters.

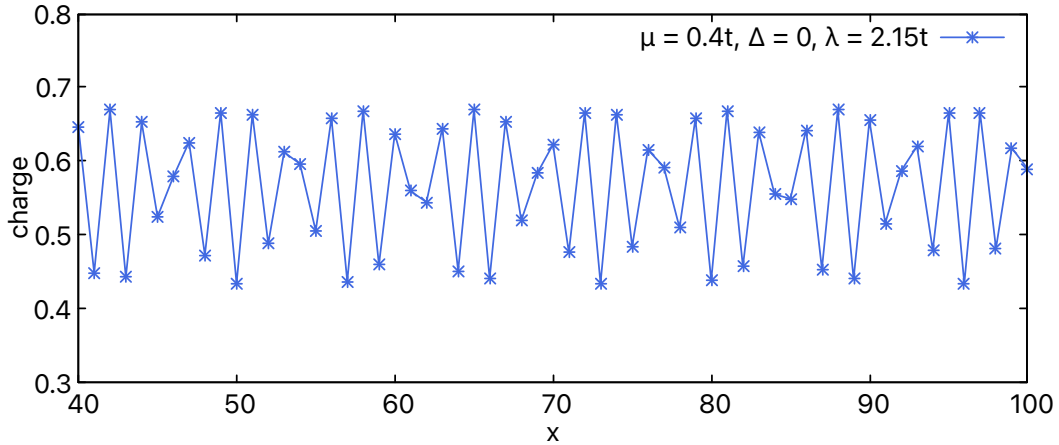


**Figure 3.8.** A CDW generated by CKM. Here,  $\mu = 0.4t$ ,  $\Delta = 0$ ,  $\lambda = 2.15t$ ,  $t = 1$ ,  $N = 200$  and  $n = 0.57$ . The charge is expressed in units of the electron charge  $e$ . The CDW shown here results from computational minimization of the free energy.

As stated at the beginning of this chapter, our objective is not to provide a comprehensive analysis of all possible phases or CDW types in this system. Rather,



our goal is to identify the regions where the system disfavors the emergence of either the topological or non-topological phase of the original Kitaev model. In this way, we can freely focus on the behavior and stability of these original Kitaev phases without the interference of other competing phases. The emergence of these competing phases is clearly defined by equation (3.16).

## 3.2 Responses to Changing Electron Density

Having found the conditions for which CKM forms different phases and CDWs, governed by equation (3.16), we can now proceed to identify the rest of the phases at various electron densities. Our main objective is to identify those phases that meet the topological criterion for the presence of zero-mode MFs.

This thesis focuses exclusively on the homogeneous phase and the dimerized phase, as they are the most commonly observed phases within the system. Consequently, the proposition made at half filling to search for analytical solutions in reciprocal space for  $X_l$ , as given by equation (2.4), remains of interest even outside of half filling.

### 3.2.1 The Minimization of the Helmholtz Free Energy

To determine the preferred phase for system construction under specific parameters, we adopt the method described in Chapter 2. Let's consider the Hamiltonian (2.1) with  $X_l$  of the form (2.4). Without neglecting any terms, the resulting Hamiltonian in the Bogoljubov-de Gennes form in momentum space is:

$$H = \sum_{k \in D} \Psi_k^\dagger \mathcal{H}_{\text{BdG}}(k) \Psi_k - \frac{1}{2} \tilde{\mu} + \frac{1}{2} N K (X_0^2 + X^2) \quad (3.17)$$

Where the Nambu vector is the same as (2.9) and the Bogoljubov-de Gennes Hamiltonian  $\mathcal{H}_{\text{BdG}}(k)$  is:

$$\mathcal{H}_{\text{BdG}}(k) = \begin{pmatrix} \xi_k - \frac{\tilde{\mu}}{2} & \frac{gX}{2} & -i\Delta_k & 0 \\ \frac{gX}{2} & \xi_{k+\frac{\pi}{a}} - \frac{\tilde{\mu}}{2} & 0 & -i\Delta_{k+\frac{\pi}{a}} \\ i\Delta_k & 0 & -(\xi_k - \frac{\tilde{\mu}}{2}) & -\frac{gX}{2} \\ 0 & i\Delta_{k+\frac{\pi}{a}} & -\frac{gX}{2} & -(\xi_{k+\frac{\pi}{a}} - \frac{\tilde{\mu}}{2}) \end{pmatrix} \quad (3.18)$$

In this last matrix, we defined  $\xi_k = -t \cos(k)$ ,  $\tilde{\mu} = \mu - gX_0$  and  $\Delta_k = \Delta \sin(k)$ . Diagonalizing (3.18) yields the energy spectrum of the electrons:

$$E_k^{\eta, \nu} = \eta \sqrt{\xi_k^2 + \Delta_k^2 + \left(\frac{\tilde{\mu}}{2}\right)^2 + \left(\frac{gX}{2}\right)^2} + \nu \sqrt{(\xi_k \tilde{\mu})^2 + (gX \Delta_k)^2 + \left(\frac{gX \tilde{\mu}}{2}\right)^2} \quad (3.19)$$

Where  $\eta = \pm 1$  &  $\nu = \pm 1$  And finally the grand canonical potential per lattice site for  $T \rightarrow 0K$  is:

$$\omega = -\frac{1}{N} \sum_{\nu, k \in D} E_k^{+, \nu} - \frac{1}{2} \tilde{\mu} + \frac{1}{2} N K (X_0^2 + X^2) \quad (3.20)$$

Given that the Helmholtz free energy is  $F = \Omega + \mu N_e$ <sup>1</sup>, we study the free energy per lattice site  $f = F/N$ . This approach enables us to introduce the electron density

<sup>1</sup>Where  $N_e$  is the number of electrons in the system.

as  $n = N_e/N$ , transforming  $f$  into:

$$f = \omega + \mu n \quad (3.21)$$

Having the free energy per lattice site, the next step is to compare the two global minima of both the dimerized and homogeneous phases. Whichever phase has a lower free energy will be the phase that the system adopts. The free energy per lattice site  $f = f(\lambda, \Delta, n|\mu, X_0, X)$  is considered with fixed values of  $\lambda$  and  $\Delta$ . We identify its minima by identifying where its gradient  $\nabla f$  vanishes, where  $\nabla = (\partial_\mu, \partial_{X_0}, \partial_X)$ . This translates to:

$$\begin{aligned} -\partial_\mu \omega &= n \\ \partial_{X_0} \omega &= 0 \\ \partial_X \omega &= 0 \end{aligned} \quad (3.22)$$

and they give three dependent minimization equations:

$$\begin{aligned} n &= \frac{1}{2} + \frac{\tilde{\mu}}{2N} \sum_{\nu, k \in D} \frac{1}{E_k^{+, \nu}} \left[ \frac{1}{2} + \nu \frac{\xi_k^2 + \left(\frac{gX}{2}\right)^2}{\sqrt{(\xi_k \tilde{\mu})^2 + (gX \Delta_k)^2 + \left(\frac{gX \tilde{\mu}}{2}\right)^2}} \right] \\ X_0 &= -\frac{g}{K} n \\ X &= \frac{g}{2NK} \sum_{\nu, k \in D} \frac{1}{E_k^{+, \nu}} \left[ \frac{gX}{2} + gX \nu \frac{\Delta_k^2 + \left(\frac{\tilde{\mu}}{2}\right)^2}{\sqrt{(\xi_k \tilde{\mu})^2 + (gX \Delta_k)^2 + \left(\frac{gX \tilde{\mu}}{2}\right)^2}} \right] \end{aligned} \quad (3.23)$$

### 3.2.2 Solutions to Minimization equations

Given the minimization equations, we can explore them to find the solutions for  $\tilde{\mu}$ ,  $X_0$  and  $X$ . First, we notice that by setting  $\tilde{\mu} = 0$  the first equation indicates that the system is at half-filling, while the third equation reduces to the self-consistency equation (2.18). The second equation provides an analytic solution for  $X_0$ . This allows us to establish a direct relationship between  $\tilde{\mu}$  and  $\mu$ , that is:

$$\tilde{\mu} = \mu + \frac{g^2}{K} n \quad (3.24)$$

Using this solution, the free energy per lattice site becomes:

$$f = -\frac{1}{N} \sum_{\nu, k \in D} E_k^{+, \nu} + \frac{1}{2} K X^2 - \tilde{\mu} \left( n - \frac{1}{2} \right) - \frac{g^2 n^2}{2K} \quad (3.25)$$

Having determined the expression of the free energy, the next step is to solve the first and third equations of minimization in (3.23), which depend only on  $\tilde{\mu}$  and  $X$ . By performing numerical computations, we can solve these equations and use the obtained results to calculate the corresponding free energies of the dimerized phase -  $f(\lambda, \Delta, n|\mu, X_0, X)$  and homogeneous phase -  $f(\lambda, \Delta, n|\mu, X_0, X = 0)$ . With this done, we can make  $\mu$ - $n$  plots where we can study the formation of the two phases. Let's examine only the formation of the dimerized phase, see Figures 3.9. These figures indicate that near half filling, for a fixed  $\Delta$ , as we increase the strength of the coupling, that is as  $\lambda$  grows, the dimerized phase becomes more stable. In other words, for a given  $\lambda$ , there exists a sufficiently large  $\Delta$  that will eliminate dimerization, similar to what occurs in the half filling case (2.4) and in the case of CDWs formation (3.7).

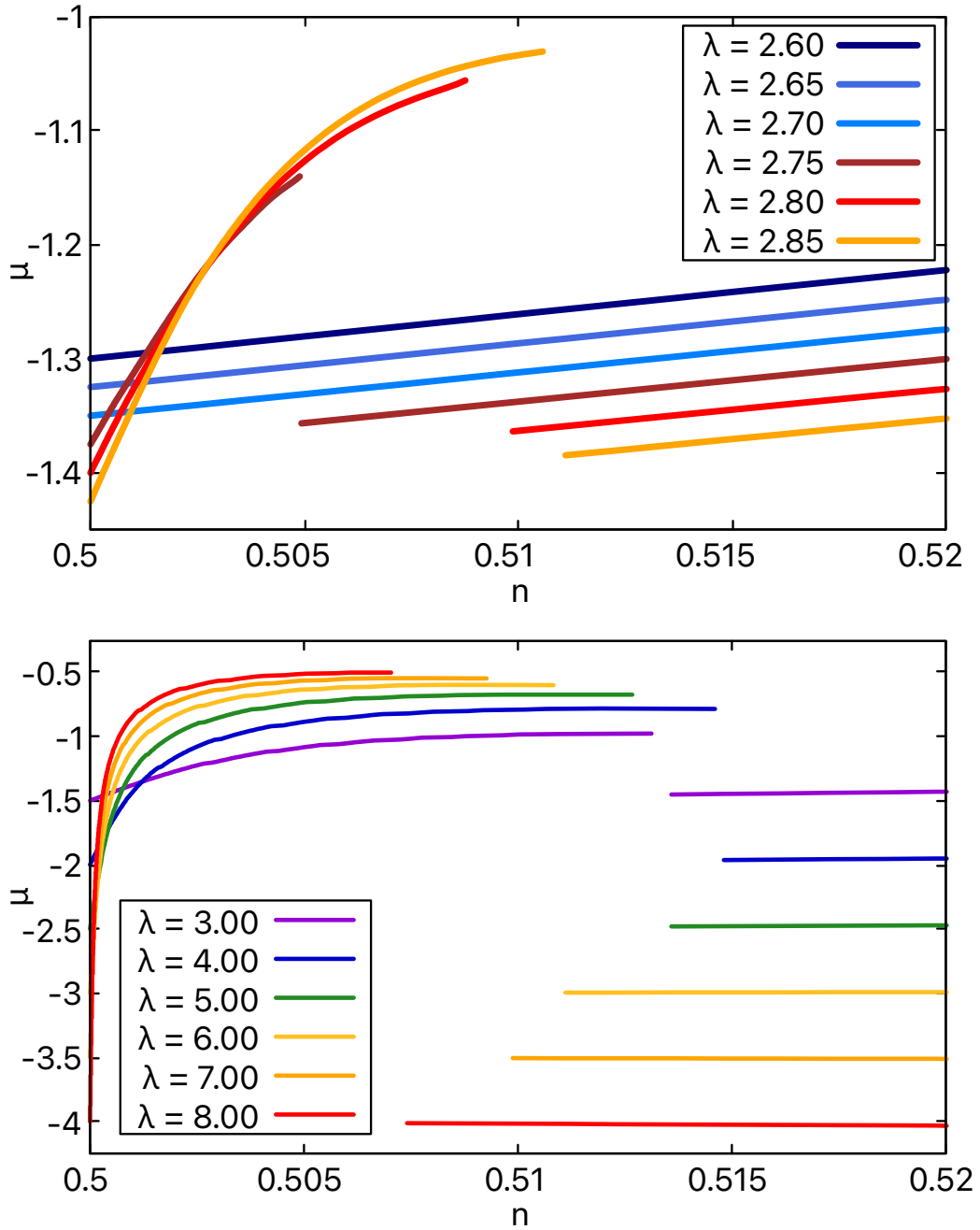


**Figure 3.9.** The chemical potential  $\mu$  versus the density of electrons  $n$  for different values of  $\lambda$  at fixed  $\Delta = 0.2t$ . In both figures, the dimerized phase appears to the left of the discontinuity in  $\mu$ . In the upper figure, the regions shaded in blue represent the non-dimerized phase, the others construct close to half filling. The figure bellow indicates that the dimerized phase persists always near half filling as  $\lambda$  increases.

Lets take a sufficiently large  $\Delta$ , to assure that a dimerized phase will not be formed and study the topology of the homogeneous phase, see Figure 3.10. An interesting observation in the Figure 3.10 is that the transition from the topological phase to the non-topological phase occurs at a fixed density, independent of  $\lambda$ .

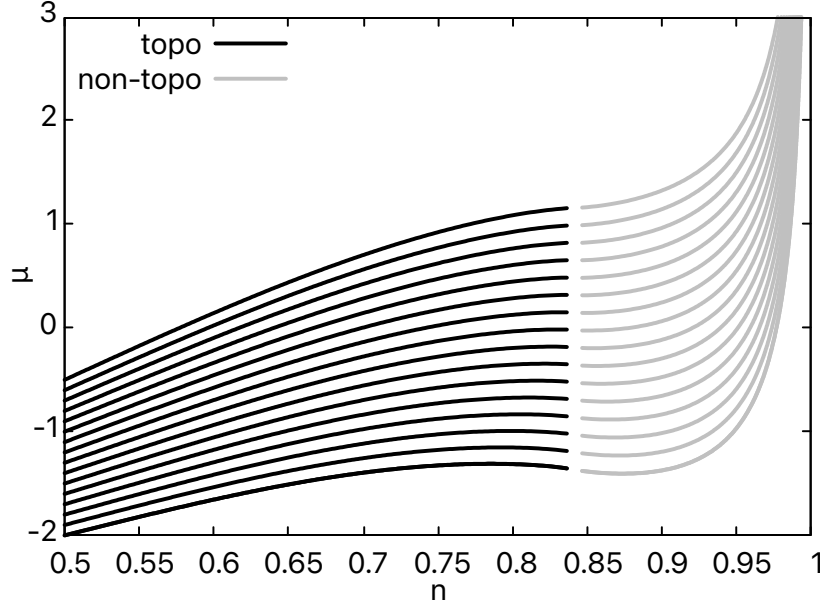


**Figure 3.10.** The chemical potential versus the density of electrons  $n$  at  $\Delta = 0.8t$  and for several values of  $\lambda$  from  $\lambda = 1.00$  (top curve) to  $\lambda = 4.00$  (bottom curve). On the gray curves (non-topo) the topological criterion is not verified while it is on the black curves (topo).

This can be explained by the behavior of CKM, which, when it tends to construct a homogeneous phase, it behaves identically to the Kitaev model, but with a redefined chemical potential  $\tilde{\mu}$ , recall equation (2.2). If CKM mirrors the Kitaev model, we would expect the phase transition between the topological and non-topological phases to occur when  $|\tilde{\mu}| = 2t$ . Now recall the first equation in the equations of minimization (3.23). This equation demonstrates that, in the absence of dimerization,  $n = n(\tilde{\mu}, \Delta)$ . Setting  $\tilde{\mu} = 2t$  eliminates the dependence on  $\lambda$ , yielding the density at which the phase transition between the two different topologies occurs:

$$n = \frac{1}{2} + \frac{1}{2N} \sum_k \frac{1}{\sqrt{1 + \left[ \frac{\Delta}{t} \frac{\sin(k)}{2 \sin^2(k/2)} \right]^2}} \quad (3.26)$$

Given the equation relating  $\tilde{\mu}$  and  $\mu$  from (2.2), we can also determine the analytical point for  $\mu$  where the change of topologies occurs. Unlike the density of electrons, the chemical potential depends on the coupling constant:

$$\mu = 2t - \frac{g^2}{K} \left\{ \frac{1}{2} + \frac{1}{2N} \sum_k \frac{1}{\sqrt{1 + \left[ \frac{\Delta}{t} \frac{\sin(k)}{2 \sin^2(k/2)} \right]^2}} \right\} \quad (3.27)$$

Having established the relationship between the chemical potential and electron density from Figures 3.9 and 3.10 for both the homogeneous and dimerized phase, we can proceed in the next chapter with the constructions of phase diagrams. These diagrams will assist us in identifying the regions where we expect to find zero-mode MFs.

## Chapter 4

# Majorana Zero Modes in the Model

For each parameter  $\mu, \Delta, \lambda$  that influences the Hamiltonian of the CKM model, we can identify various phases it can generate at temperatures near absolute zero. The phases are: a topological homogeneous phase, a non-topological homogeneous phase, a non-topological dimerized phase, or other non-topological CDWs. However, like in any  $\mu$ - $n$  diagram, there are regions where two or more phases can coexist. These regions are characterized by horizontal plateaus where the chemical potential remains constant while the electron density varies. We want to delineate these coexistence regions to understand when our system forms either a single topological phase or a mixture of phases with diverse topologies. This is significant because we demonstrated that the presence of zero-mode Majoranas depends on these conditions, recall Figures 1.5 and 1.11. We also note the significant influence of boundary conditions on the system, whether they are open or closed, as shown in Figure 1.6.

Having constructed these phase diagrams and identified whether we are in a coexisting region of different phases or a single phase, for each value of  $\mu, \Delta$  and  $\lambda$ , we will employ computational methods. Specifically, we will minimize the free energy, after allocating random values to  $X_l$  in real space, by diagonalizing Hamiltonian (2.1). This approach aims to converge to the minima of the free energy, thus confirming the conclusions drawn from the phase diagrams. Additionally, we will present probability density functions illustrating the occurrence of zero-mode MFs in the system.

### 4.1 The Phase Diagrams

As discussed in the introduction of this chapter, constructing phase diagrams requires identifying the regions where different phases can coexist. This formal study of phase coexistence regions was pioneered by the Scottish physicist James Clerk Maxwell in 1875. His work laid the foundation for understanding phase equilibrium, particularly through what is now known as Maxwell's construction [41].

Let's first consider the generic  $\mu$ - $n$  diagram for the parameters  $\Delta$  and  $\lambda$  when both the homogeneous and dimerized phases are present in the system, see Figure 4.1. In this figure, we observe two phase transitions. Moving away from half-filling, the system undergoes a transition from a non-topological dimerized phase to a topological homogeneous phase. At higher electron densities, the system transitions from a topological homogeneous phase to a non-topological homogeneous phase. Consequently, two Maxwell constructions are required to describe these phase

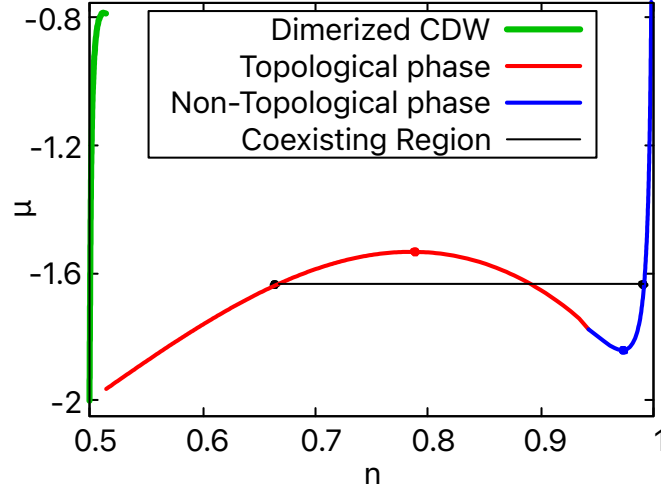


**Figure 4.1.**  $\mu$ - $n$  diagram and Maxwell's construction for the transition between topological and non-topological homogeneous phases with  $\Delta = 0.20t$ ,  $\lambda = 4.00t$ , and  $t = 1$ . The green line represents the Dimerized CDW phase, the red line indicates the topological homogeneous phase, and the blue line denotes the non-topological homogeneous phase. The coexistence region during the topological transition is represented by the black line and is bordered by the black points. Spinodal points for each phase are marked in their respective colors.

transitions. Let's examine the procedure for Maxwell's construction around the topology transition in the homogeneous phases: the local minima  $\mu_{\min}$  and maxima  $\mu_{\max}$  represent the spinodal points. The beginning and end of the coexistence regions occur when there exists two electron densities  $n_1$  and  $n_2$  corresponding to the same  $\mu_M \in (\mu_{\min}, \mu_{\max})$  such that the area above the line  $\mu = \mu_M$ , bounded by the  $\mu(n)$  curve, is equal to the area below the line, also bounded by the  $\mu(n)$  curve. An interesting aspect of Maxwell's construction is its ability to determine the percentage of each phase present within the coexistence region. For instance, if the system's electron density is  $n \in (n_1, n_2)$ , and we denote the percentage of the occupied topological phase in the system by  $r$ , then the percentage of the non-topological phase occupied in the system will be  $1 - r$ , where:

$$r = \frac{n_2 - n}{n_2 - n_1} \quad (4.1)$$

The same process must be repeated for the phase transition between the dimerized phase and the homogeneous phase. By doing this, we construct the phase diagram that shows the transitions of the dimerized and homogeneous phases and their topologies. However, we also know that for a given  $\lambda$ , the system forms CDWs up to a certain  $\Delta$ , as shown in Figure 3.7. In the phase diagram, we can draw a curve representing the spinodal region, below which the system predominantly favors the formation of CDWs. This curve is defined by equation (3.16).

With all these considerations, we are finally able to construct phase diagrams  $\Delta$  versus  $n$  at fixed  $\lambda$ , see Figures 4.2, 4.3, 4.4 and for a detailed view of the dimerized-homogeneous transition, refer to the zoomed-in Figure 4.5, as it is not clearly visible in the other figures.

**Figure 4.2.** Phase diagram  $\Delta$  versus  $n$  for  $\lambda = 0$ ,  $t = 1$ . This is the limiting case where CKM coincides with the Kitaev Model. In this scenario, dimerization is absent, and the change in the topological criterion occurs through a continuous transition without any coexistence region.

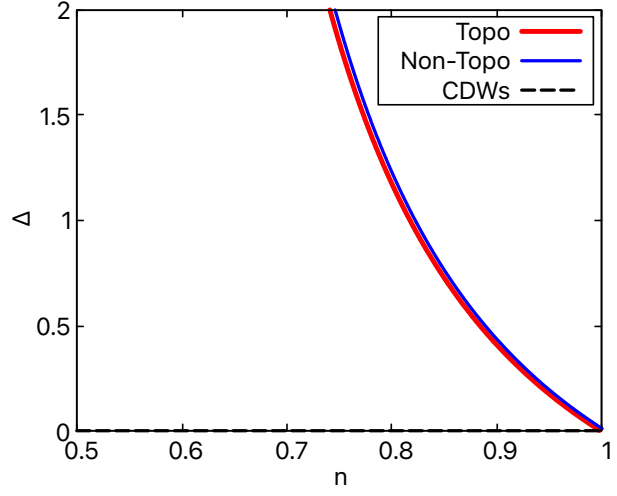


**Figure 4.3.** Phase diagram  $\Delta$  versus  $n$  for  $\lambda = 2t$ ,  $t = 1$ . In this scenario, dimerization is present for small  $\Delta$  in the vicinity of half filling. The interaction with the field introduces a coexistence region between the two topological phases.

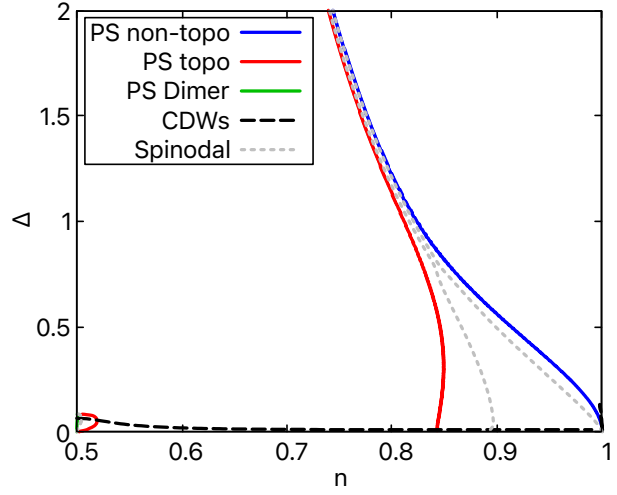


**Figure 4.4.** Phase diagram  $\Delta$  versus  $n$  for  $\lambda = 4t$ ,  $t = 1$ . Here, the dimerization becomes more pronounced while still remaining near half filling. The coexistence region widens and the phase separation occurs at lower density.

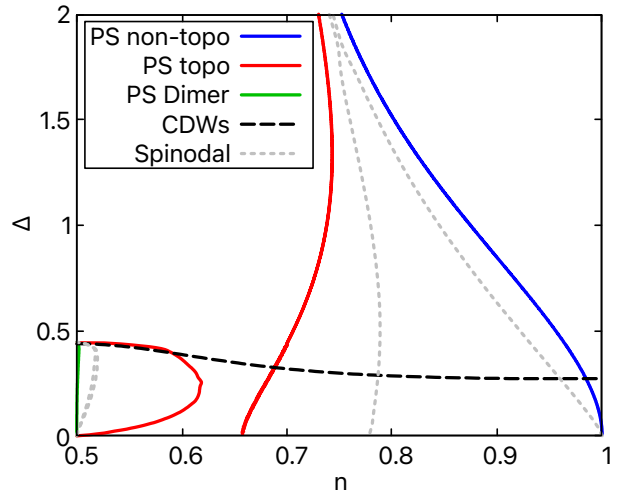
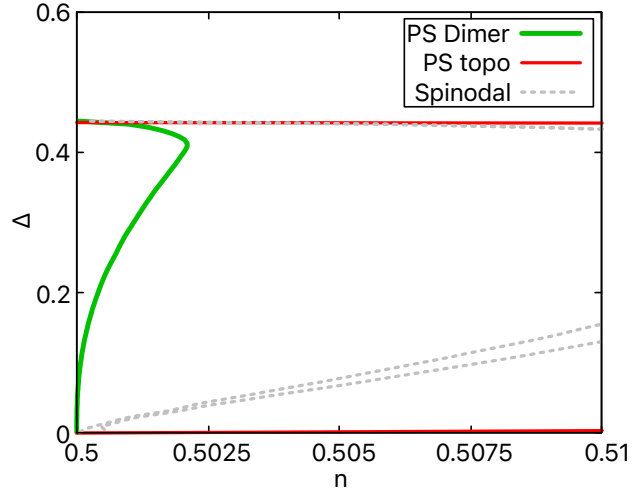


**Figure 4.5.** Phase diagram  $\Delta$  versus  $n$  for  $\lambda = 4t$ ,  $t = 1$ . Here, only the phase separation between the non-topological dimerized phase and the topological homogeneous phase is depicted. The dimerized phase tends to form only near half-filling and is not favored at densities further away.



In these diagrams, phase separation is depicted as follows: the blue line marks the boundary separating the non-topological phase, the red line denotes the boundary separating the topological phase, and the green line indicates the boundary of the non-topological dimerized phase. The grey dotted lines represent the spinodal lines, while in the region underneath the black dashed line the formation of non-topological CDWs, or potential different phases, is favored. Note that our model Hamiltonian is particle-hole symmetric, so the range for  $n \in (0, 0.5)$  mirrors the range  $n \in (0.5, 1)$ . The phase diagrams show that without the coupling field, there is no phase separation between the topological and non-topological phases; the system is entirely in either the topological phase or the non-topological phase (Figure 4.2). The curve where the phase transition occurs is the analytical expression in equation (3.26).

When  $\lambda > 0$ , phase separation emerges at high densities, and the dimerized phase forms immediately near half-filling for small  $\Delta$  (Figure 4.3). As  $\lambda$  increases, the coexistence region broadens, and phase separation occurs at lower densities (Figure 4.4). The dimerized phase also becomes more evident as  $\lambda$  grows but remains always limited to a region near half filling (Figure 4.5).

Having established these phase diagrams, we can now proceed to the computational analysis in real space to investigate the presence of zero-mode MFs in various scenarios.

## 4.2 Majorana Fermions in Single Phases

Let's first consider the scenario where the system forms either a topological phase or a non-topological phase. This occurs when the parameters  $\lambda$ ,  $\Delta$ , and  $n$  are outside the Maxwell coexistence region of phases. Among the three possible phases, non-topological dimerized, non-topological homogeneous, and topological homogeneous, only the topological homogeneous phase hosts zero-mode MFs. The presence of the MFs in the topological homogeneous phase depend on the boundary conditions of our chain, whether they are open or closed. With open boundary conditions, the unpaired Majorana zero-modes are located at the edges of the chain and do not meet each other, preventing annihilation and making them detectable. However, with closed boundary conditions, the edges of the chain are connected, causing the unpaired MFs to pair up and annihilate, see Figure 4.6 and recall Figure 1.6.



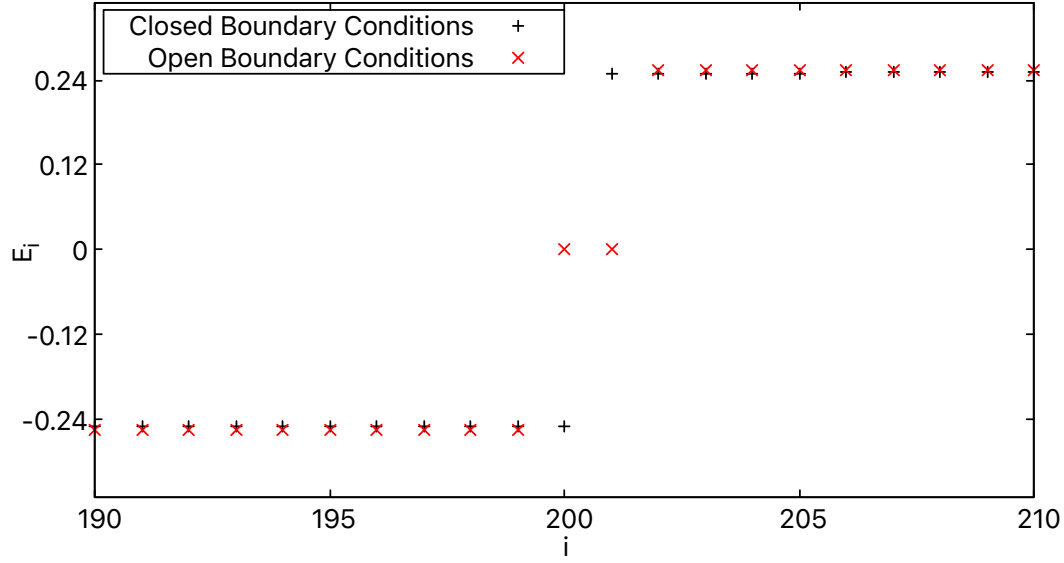


**Figure 4.6.** The energy spectrum at the electron density  $n = 0.75$  for  $\Delta = 0.5t$ ,  $\lambda = 2t$ ,  $t = 1$  and  $N = 200$ ; here,  $i = 0, \dots, 2N - 1$  labels the energy levels in increasing order. For open boundary conditions, zero-mode MFs are present. For closed boundary conditions, zero-mode MFs are absent.

Ideally, we want a system where we don't have to worry about whether the boundary conditions in our system are open or closed. The solution to this problem is to look for MFs in the regions between coexisting phases with different topologies (see the following section).

### 4.3 Majorana Fermions at Interfaces of Coexisting Phases

It is well established that MFs are located at the interfaces of different topological regions within the system, as discussed in Section 1.4. The coupling field with the electrons shows that as this coupling increases, the region of coexisting phases expands correspondingly, as illustrated in Figures 4.2 - 4.5.

These figures illustrate two distinct coexisting regions: the first region is a coexistence between a non-topological homogeneous and a topological homogeneous phase, while the second region is between a non-topological dimerized phase and a topological homogeneous phase. We have determined the percentage presence of each phase in the system, as described by equation (4.1). However, while the minimum free energy is realized when the two separated phases are macroscopic, each confined into a single region, a one-dimensional system will likely segment them into different sections along the chain, potentially creating multiple interfaces and consequently more MFs will be present, see Figure 4.7. The reason for this behavior is that in one dimension the energy cost to create an interface is never macroscopic.

We observe two distinct types of interfaces. The first is the NTT interface, where a non-topological phase encounters a topological phase. The second is the TNT interface, where a topological phase encounters a non-topological phase. The key difference between these interfaces lies in the type of MF they leave unpaired, as illustrated in the Figure 4.8.

We define an *NTT MF* as a MF appearing at the NTT interface, and a *TNT MF* as

a MF appearing at the TNT interface. Let's analyze these two distinct coexisting

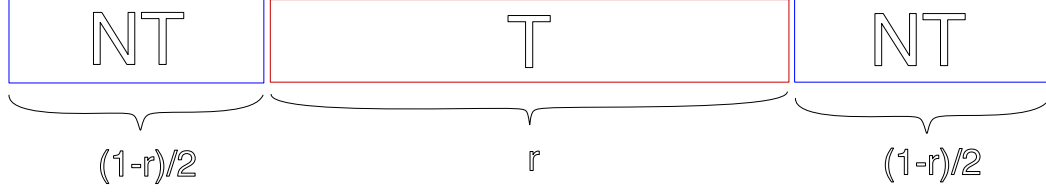
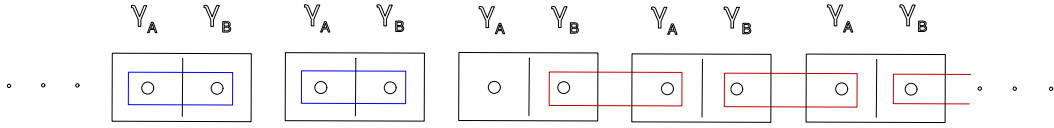
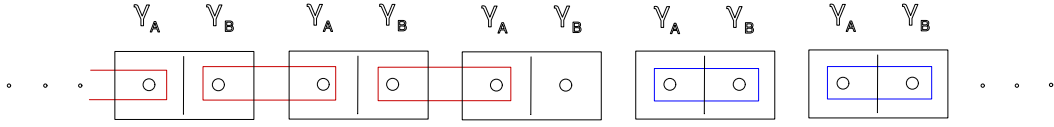


**Figure 4.7.** A possible configuration illustrating the coexistence of topological and non-topological phases is shown. The red rectangles marked with a  $T$  represent the topological phase, occupying a fraction  $r$  of the system. Conversely, the blue rectangles marked with  $NT$  represent the non-topological phase, which occupies the remaining  $1 - r$  fraction of the system.



(a) NTT Interface



(b) TNT Interface

**Figure 4.8.** Illustration of the NTT (figure a) and TNT (figure b) interfaces using domino tiles. The red pairings of the MFs indicate the topological phase, while the blue pairings indicate the non-topological phase. At the NTT interface, the  $\gamma_A$  MF is left unpaired, whereas in the TNT interface, the  $\gamma_B$  MF is left unpaired.

phases to locate where MFs appear and observe the charge modulation to determine their topologies using computational methods.

### 4.3.1 Non-Topo-Homogeneous and Topo-Homogeneous Coexistence

Let's consider CKM with closed boundary conditions,  $\lambda = 4t$ ,  $\Delta = t$ ,  $t = K = a = 1$ , a chain with  $N = 512$  sites and a filling of electrons at  $n = 86\%$ . Given these conditions, we anticipate the presence of two homogeneous coexisting phases with distinct topologies. The computational approach in real space, which involves minimizing the free energy, yields the results displayed in Figures 4.9 - 4.12. The displacement variable  $X_l$ , shown in Figure 4.9, assumes two specific constant values. These values of  $X_l$  lead to the spectrum obtained from the numerical diagonalization of the  $2N \times 2N$  Hamiltonian  $H_{\text{BdG}}$ , as shown in Figure 4.10.

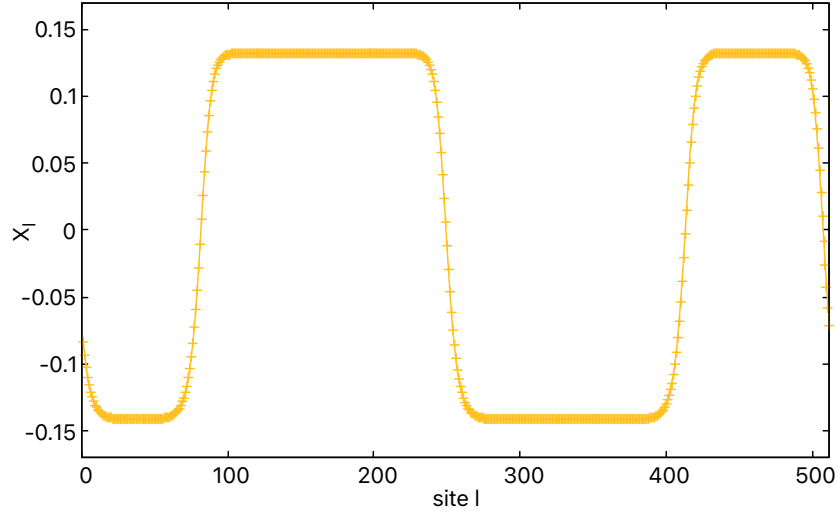


**Figure 4.9.** The displacement variable  $X_l$  of the field at every site  $l$ . Here every site is shifted by the transformation  $X_l \rightarrow X_l - (n \cdot g/K)$ . The system constructs two constant values of  $X_l$ .

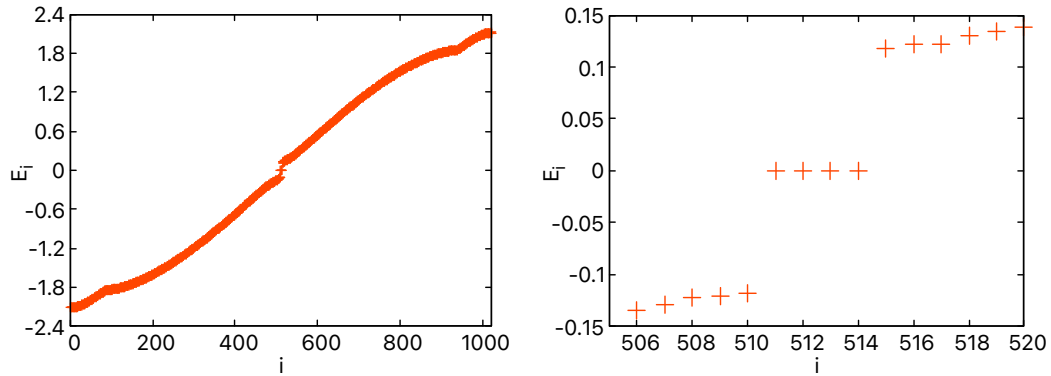


**Figure 4.10.** The energy spectrum. Here,  $i = 0, \dots, 2N - 1$  labels the energy levels in increasing order. The figure on the left shows the complete energy spectrum. The figure on the right shows that the system admits a four-degenerate zero-mode.

The spectrum admits four-degenerate zero-mode which indicate the presence of 4 MFs. The topology can be seen in the charge modulation inside the system in Figure 4.11: we find two topological regions and two non-topological regions. Therefore,

the 4 MFs will be localized at the 4 interfaces. Depending on the type of interface, a different type of MF will be left unpaired, see Figure 4.12.

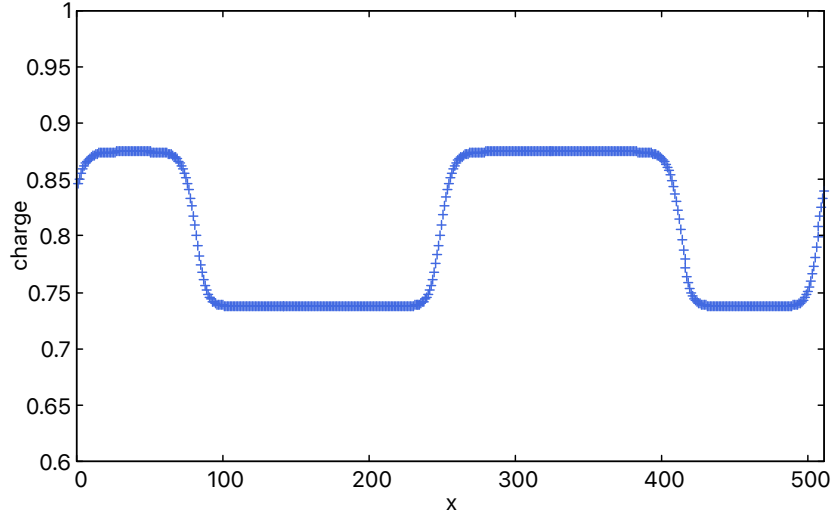


**Figure 4.11.** Charge modulation in the system. The charge is expressed in units of the electron charge. Regions with lower constant charge denote the topological phase, while those with higher charge indicate the non-topological phase.

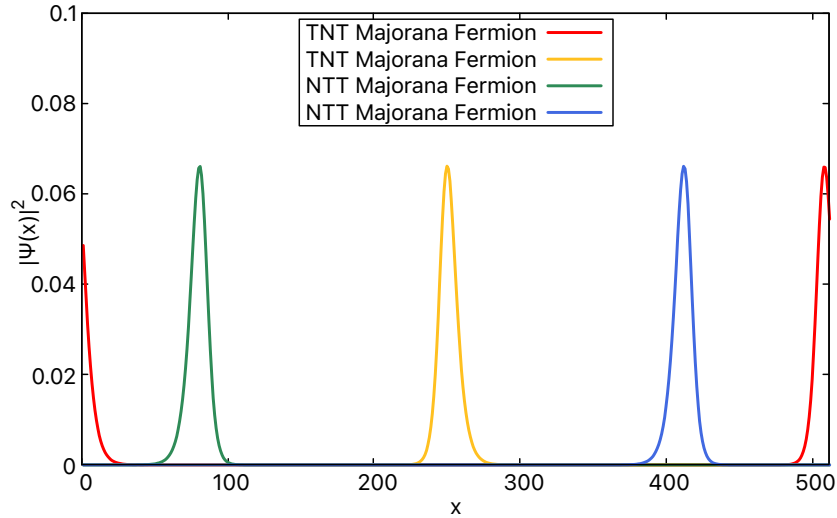


**Figure 4.12.** The localized Majorana zero-modes. The figure shows the square amplitude of the wave functions. All the MFs of different types are located at the interfaces between two different topologies.

Four MFs are observed at the interfaces where there is a change in the system's topology. The same result would be obtained if open boundary conditions were applied<sup>1</sup>.

<sup>1</sup>One might argue that with open boundary conditions, if an edge of the chain happens to be in a topological phase, an additional MF would be found at that edge.

### 4.3.2 Non-Topo-Dimerized and Topo-Homogeneous Coexistence

Let's consider a coexisting phase of a non-topological dimerized phase and a topological homogeneous phase. For this coexistence we take  $\lambda = 4t$ ,  $\Delta = 0.4t$ ,  $t = K = a = 1$ , a chain with  $N = 512$  sites and a filling of electrons at  $n = 57\%$ . The computational approach yields the Figures 4.13 - 4.16. The displacement variable  $X_l$ , shown in Figure 4.9, assumes two forms: a centered constant region and two dimerized regions at the edges. This configuration of  $X_l$  gives the spectrum shown in Figure 4.10.

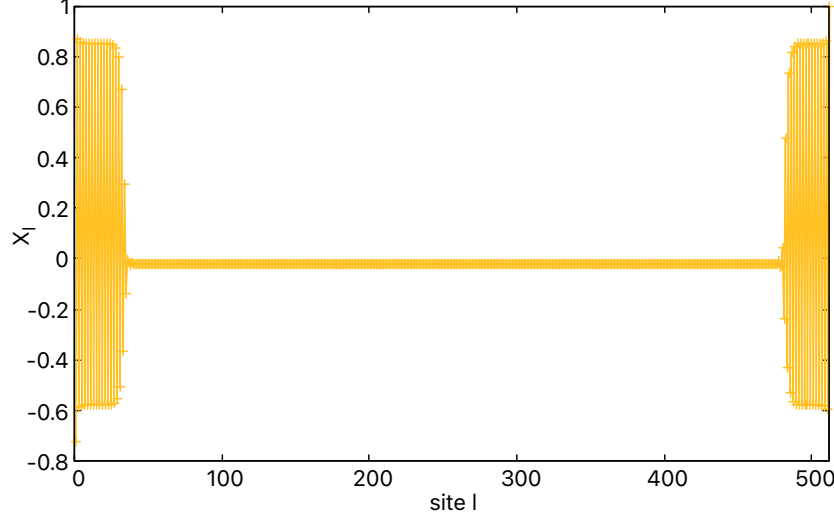


**Figure 4.13.** The displacement variable  $X_l$  of the field at every site  $l$ . Here every site is shifted by the transformation  $X_l \rightarrow X_l - (-n \cdot g/K)$ . The system constructs two regions with alternating  $X_l$  and one region with a constant value of  $X_l$ .

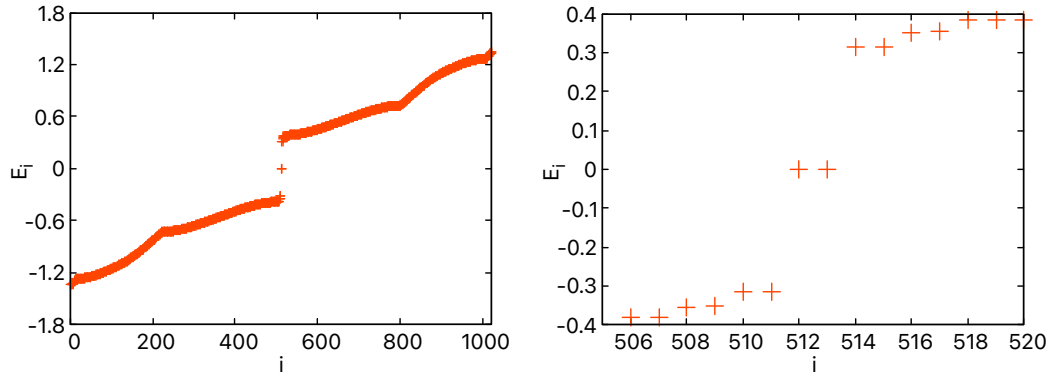


**Figure 4.14.** The energy spectrum. Here,  $i = 0, \dots, 2N - 1$  labels the energy levels in increasing order. The figure on the left shows the complete energy spectrum. The figure on the right shows that the system admits a two-degenerate zero-mode.

The spectrum admits two-degenerate zero-mode which indicate the presence of 2 MFs. The topology can be seen in the charge modulation inside the system in Figure 4.11: we find one topological region and two non-topological dimerized regions. Therefore, the 2 MFs will be localized at the 2 interfaces.

Depending on the type of interface, a different type of MF will be left unpaired, see Figure 4.12.

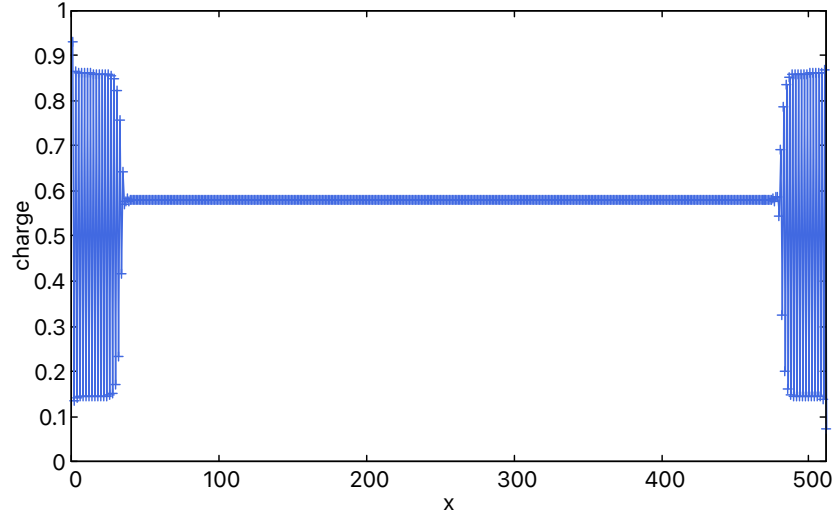


**Figure 4.15.** Charge modulation in the system. The charge is expressed in units of the electron charge. Regions with alternating charge denote the non-topological dimerized phase, while those with constant charge indicate the topological phase.

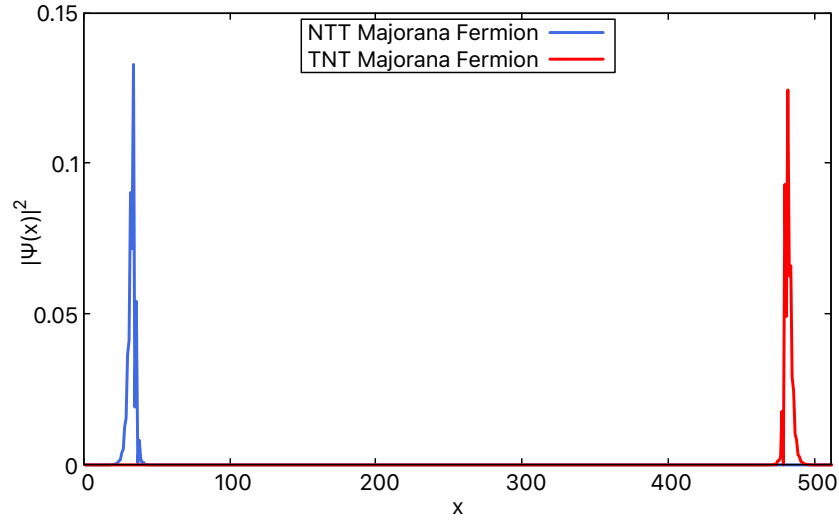


**Figure 4.16.** The localized Majorana zero-modes. The figure shows the square amplitude of the wave functions. The MFs are located at the interfaces between two different topologies.

Two MFs are observed at the interfaces where there is a change in the system's topology.<sup>2</sup>

---

<sup>2</sup>The same result would be obtained with closed boundary conditions. However, due to the current structure of the minimization program, it does not obtain it.

# Conlcusions

Detecting MFs in condensed matter physics is inherently challenging, especially when aiming to realize the ideal conditions described by the Hamiltonians of topological superconductors, which are essentially theoretical models. Achieving such a superconductor typically demands materials with rare combinations of properties, including the ability to induce superconductivity through proximity effects. Moreover, 1D superconductors, often implemented in nanowires, require precise fabrication techniques to achieve the necessary structural and electronic properties. Furthermore, maintaining the superconducting state essential for Majorana modes necessitates extremely low temperatures, approaching absolute zero. MFs manifest as zero-modes and are difficult to be distinguished from other low-energy excitations present in the system. These factors collectively contribute to the formidable challenges in observing and confirming the existence of MFs in experimental setups.

Despite the complexity with creating systems that can host zero-mode MFs, our determination to pursue them persists. We understand very well their anticipated locations within topological system: they reside at the edges of topological superconductors or at interfaces where a change in topology occurs. The appearance of these MFs in such cases occurs because they remain left out in the system, unpaired with any other MF and therefore isolated. This condition is significant as MFs typically appear in pairs due to their intrinsic nature ob being the two halves of an electron.

The Kitaev model serves as the most elementary representation of a topological superconductor. It exhibits a binary nature, existing either entirely within a topological phase capable of hosting zero-modes Majoranas at the chain edges, or entirely within a non-topological phase. Detecting MFs at the edges has proven challenging due to the specific configurations required for their observation. We couple the Kitaev Model with a classical elastic field, incorporating a linear term that relates the field variable to the electron density at each site. This setup allows us to efficiently manipulate the electron density within the system.

By introducing the classical elastic field to the Kitaev model, we pay the price of encountering different behaviors in the system. The first noticeable occurring effect is the formation of a dimerized phase at half filling, i.e., a CDW. This happens due the fact that as soon as the coupling with the field is turned on, a nesting of the Fermi surface occurs. This on its own causes a symmetry breaking which by principle in topology must mean that there must be a phase transition to a different topology. Indeed a first-order phase transition occurs between the non-topological dimerized phase and the topological superconducting phase.

Studying this new model in real space reveals regions where the system generates CDWs and other phases. By examining the electronic susceptibility and applying the

random phase approximation for the system, we have identified strategies to avoid these non-topological CDWs and other phases. Specifically, our findings demonstrate that for a given coupling constant  $\lambda$ , there exists a sufficiently large superconducting parameter  $\Delta$  that prevents the formation of this unwanted region. Below this  $\Delta$ , both phases compete for dominance within the system, with the CDW phase prevailing as  $\Delta$  approaches zero.

The main distinction between the Kitaev model and this new model lies in the emergence of coexisting regions between the topological and non-topological phases as soon as the coupling constant  $\lambda > 0$ . As  $\lambda$  increases, these coexisting regions expand. This development is particularly significant in the search for MFs, as we know that interfaces between different topological phases within these regions host zero mode MFs. Furthermore, there is no concern regarding the boundary conditions of the 1-dimensional chain because MFs at interfaces are invariant on those conditions.

In theory and through numerical computations, we demonstrate the existence of these coexisting regions and establish that the number of interfaces between the two distinct topologies in the system corresponds to the number of zero-mode MFs. In practical terms, the classical elastic field can be interpreted similarly to the classical phonon field, where the field variable  $X_l$  represents the average displacement of atoms within the chain. Under this interpretation, CKM can be seen as an incomplete Holstein model. It is incomplete because CKM lacks terms describing phonons. To advance the search for MFs from this thesis, a Hamiltonian that incorporates the system's dynamics and treats the classical elastic field as the classical phonon field should be considered.



# Appendix

## Appendix A. CKM in Reciprocal Space

An example of expressing a term in a Hamiltonian in reciprocal space, that was originally written in real space, can be shown by transforming the term  $\sum_{l=0}^{N-1} (-1)^l c_l^\dagger c_l$ . To transform this term, we firstly recall the Fourier transforms of the creation and annihilation operators respectively equations (1.22) and (1.21). For this specific term we will also use the identity  $e^{i\pi} + 1 = 0$ .

$$\begin{aligned}
\sum_{l=0}^{N-1} (-1)^l c_l^\dagger c_l &= \sum_{k_j} \sum_{k_q} c_{k_j}^\dagger c_{k_q} \frac{1}{N} \sum_l e^{i(k_j - k_q)x_l} e^{i\frac{\pi}{a}x_l} = \\
&= \sum_{k_j} \sum_{k_q} c_{k_j}^\dagger c_{k_q} \frac{1}{N} \sum_l e^{i(k_j - k_q + \frac{\pi}{a})x_l} = \\
&= \sum_{k_j} \sum_{k_q} c_{k_j}^\dagger c_{k_q} \delta(k_j + \frac{\pi}{a} - k_q) = \\
&= \sum_{k_j} c_{k_j}^\dagger c_{k_j + \frac{\pi}{a}}
\end{aligned}$$

## Appendix B. The self Consistency Equation for Small X

To derive equation (2.20), take firstly equation (2.18) and do a Taylor expansion in  $X$  neglecting second and higher orders. Expanding the denominator in (2.18) gives:

$$X = \frac{g}{2NK} \sum_{k \in D} \left[ \frac{\frac{gX}{2} + \Delta_k}{\sqrt{gX\Delta_k + \Delta_k^2 + \xi_k^2 + o(x^2)}} + \frac{\frac{gX}{2} - \Delta_k}{\sqrt{-gX\Delta_k + \Delta_k^2 + \xi_k^2 + o(x^2)}} \right]$$

The dominating term in the denominator is  $(\Delta_k^2 + \xi_k^2)$ , we separate it from the infinitesimal part:

$$X = \frac{g}{2NK} \sum_{k \in D} \left[ \frac{\frac{gX}{2} + \Delta_k}{\sqrt{\Delta_k^2 + \xi_k^2} \sqrt{1 + \frac{gX\Delta_k}{\Delta_k^2 + \xi_k^2}}} + \frac{\frac{gX}{2} - \Delta_k}{\sqrt{\Delta_k^2 + \xi_k^2} \sqrt{1 - \frac{gX\Delta_k}{\Delta_k^2 + \xi_k^2}}} \right]$$

Lastly we apply the property  $(1+x)^\alpha = 1 + \alpha x + o(x^2)$  that gives a final result:

$$X = \frac{g^2 X}{2NK} \sum_{k \in D} \frac{\xi_k^2}{\sqrt{\Delta_k^2 + \xi_k^2}^3}$$

If we look for solutions where  $X \neq 0$ , then we obtain an equation:

$$1 = \frac{g^2}{2NK} \sum_{k \in D} \frac{\xi_k^2}{\sqrt{\Delta_k^2 + \xi_k^2}^3}$$

### $\Delta$ as an infinitesimal parameter

We can prove analytically equation (2.21). The sum in equation (2.20) can be transformed into a Riemann integral by increasing the number of lattice sites  $N$  to infinity. This yields:

$$1 = \frac{g^2}{4\pi K} \int_0^\pi dk \frac{\xi_k^2}{\sqrt{\Delta_k^2 + \xi_k^2}^3}$$

In this last identity, as  $\Delta \ll 1$ , an elliptical divergence occurs in the integral. This divergence occurs around the region  $k = \pi/2$ . We can treat this elliptical divergence by separating the domain of integration  $D$  into two regions: one around the region of divergence which we define as  $D^* = (\pi/2 - \epsilon, \pi/2 + \epsilon)$  and the other as the outside region  $\hat{D} = D \setminus D^*$ . These two regions  $D^*$  and  $\hat{D}$  will give two integrals with the same integrand. Each integral is treated differently. We apply the approximation  $\sqrt{1+x}^\alpha = 1 + \alpha x$  in the denominator for the integral containing the divergence, i.e., the region  $D^*$ . For the region without the divergence, i.e., the region  $\hat{D}$ , we expand the integrand in a Taylor series up to the second order. These considerations yield the last expression in units of  $t$ :

$$\frac{2}{\lambda} = \frac{1}{2\pi} \int_{D^*} dk \frac{|\frac{\pi}{2} - k|}{(\frac{\pi}{2} - k)^2 + \frac{3}{2}\Delta^2} + \frac{1}{2\pi} \int_{\hat{D}} dk \left(1 + \frac{1 - 3\Delta^2}{2} k^2\right)$$

A compact analytical expression is:

$$\frac{2\pi}{\lambda} = \frac{1}{2} \log \left(1 + \frac{2\epsilon^2}{3\Delta^2}\right) + \frac{\pi}{2} - \epsilon + \left(\frac{1 - 3\Delta^2}{2}\right) \left(\frac{(\frac{\pi}{2} - \epsilon)^3}{3}\right)$$

This analytical expression, with  $\epsilon = 0.95$ , is used for the inset in Figure 2.5. If  $\Delta \rightarrow 0^+$  the most dominant term in the final expression becomes the logarithm. Neglecting the other terms yields a result:

$$\Delta = \epsilon \sqrt{\frac{2}{3}} \frac{1}{\sqrt{e^{\frac{4\pi}{\lambda} - A(\epsilon)} - 1}} \propto e^{-\frac{2\pi}{\lambda}}$$

Where in this last equation we defined  $A(\epsilon) = 2 \cdot (\frac{\pi}{2} - \epsilon) + \frac{2}{3}(\frac{\pi}{2} - \epsilon)^3$ .

## Appendix C. Susceptibility

The susceptibility, which is a function dependent on the wavevector  $q$ , is dependent also on the outside system parameters  $\Delta$  and  $\mu$ . Here we want to prove that the most general compact algebraic expression of the susceptibility is equation (3.7). Let's take equation (3.6) and insert in it the analytical expressions for the Green's Function and Anomalous Green's Function, respectively, equations (3.4) and (3.5):

$$\chi^T(q) = -\frac{T}{\mathcal{V}} \sum_{k, \omega_n} \frac{-i\omega_n - \xi_+}{\omega_n^2 + E_+^2} \frac{-i\omega_n - \xi_-}{\omega_n^2 + E_-^2} - \frac{\Delta_+}{\omega_n^2 + E_+^2} \frac{\Delta_-}{\omega_n^2 + E_-^2}$$

Recalling that the Matsubara frequencies for fermions are defined as  $\omega_n = (2n+1)\pi T$ , we obtain the following identity:

$$\begin{aligned} \chi^T(q) = & \frac{T}{\mathcal{V}} \frac{1}{(\pi T)^4} \sum_k \sum_{n \in \mathbb{Z}} (\pi T)^2 \frac{2n+1 - i\xi_+/\pi T}{(2n+1)^2 + (E_+/\pi T)^2} \frac{2n+1 - i\xi_-/\pi T}{(2n+1)^2 + (E_-/\pi T)^2} + \\ & + \Delta_+ \Delta_- \frac{1}{(2n+1)^2 + (E_+/\pi T)^2} \frac{1}{(2n+1)^2 + (E_-/\pi T)^2} \end{aligned}$$

These sums can be solved with the help of the Digamma function and its following properties that give two compact identities:

$$\begin{aligned} \sum_{n=-\infty}^{\infty} \frac{1}{(2n+1)^2 + A^2} \frac{1}{(2n+1)^2 + B^2} &= \frac{\pi}{2AB(A^2 - B^2)} \left[ A \tanh \frac{\pi B}{2} - B \tanh \frac{\pi A}{2} \right] \\ \sum_{n=-\infty}^{\infty} \frac{2n+1+ia}{(2n+1)^2 + A^2} \frac{2n+1+ib}{(2n+1)^2 + B^2} &= \frac{\pi}{2AB(A^2 - B^2)} \left[ -abA \tanh \frac{\pi B}{2} + abB \tanh \frac{\pi A}{2} + \right. \\ &\quad \left. + A^2 B \tanh \frac{\pi A}{2} - AB^2 \tanh \frac{\pi B}{2} \right] \end{aligned}$$

Thus giving an expression for the susceptibility at finite temperature  $T$  as:

$$\begin{aligned} \chi^T(q) = & \frac{1}{2\mathcal{V}} \sum_k \frac{1}{E_+ E_- (E_+^2 - E_-^2)} \left\{ E_- \tanh \frac{E_+}{2T} [\epsilon_+ \epsilon_- + E_+^2] - E_- \tanh \frac{E_-}{2T} [\epsilon_+ \epsilon_- + E_-^2] + \right. \\ & \left. + \Delta_+ \Delta_- [E_+ \tanh \frac{E_-}{2T} - E_- \tanh \frac{E_+}{2T}] \right\} \end{aligned}$$

In this thesis, we treat the system at the absolute zero temperature limit and therefore we have to take in this final expression the limit  $T \rightarrow 0^+$ . By doing so we use the property  $\tanh \frac{x}{T} \rightarrow \text{sign}(x)$  giving the general form:

$$\chi(q) = \frac{1}{2\mathcal{V}} \sum_k \frac{E_+ E_- - \xi_+ \xi_- + \Delta_+ \Delta_-}{E_+ E_- (E_+ + E_-)}$$

# Bibliography

- [1] E. Majorana, "Teoria simmetrica dell'elettrone e del positrone," *Nuovo Cimento*, Vol. 14, No. 4, pp. 171-184, 1937.
- [2] Deppisch, F. F., Lindner, M., Päs, H. (2017). Search for Majorana neutrinos. *Reviews of Modern Physics*, 89(1), 025004.
- [3] Alicea, J. (2012). Topological superconductors: A review. *Reports on Progress in Physics*, 75(7), 076501.
- [4] Qi, X.-L., Zhang, S.-C. (2011). Topological Insulators and Topological Superconductors. *Reviews of Modern Physics*, 83(4), 1057-1110.
- [5] Aasen, D., Hell, M., Mishmash, R. V., Higginbotham, A. P., Danon, J., Leijnse, M., ... Marcus, C. M. (2016). Milestones toward Majorana-based quantum computing. *Physical Review X*, 6(3), 031016.
- [6] M. T. Deng, S. Vaitiekenas, E. B. Hansen, J. Danon, M. Leijnse, K. Flensberg, J. Nygård, P. Krogstrup, C. M. Marcus, "Majorana bound state in a coupled quantum-dot hybrid-nanowire system", 23 December, 2016, *Science*, VOL 354 ISSUE 6319
- [7] Benjamin E. Feldman, Mallika T. Randeria, Jian Li, Sangjun Jeon, Yonglong Xie, Zhijun Wang, Ilya K. Drozdov, B. Andrei Bernevig and Ali Yazdani, "High-resolution studies of the Majorana atomic chain platform", March 2017, *Nature*, DOI: 10.1038/NPHYS3947
- [8] Seung-Hwan Do<sup>1</sup>, Sang-Youn Park, Junki Yoshitake, Joji Nasu, Yukitoshi Motome, Yong Seung Kwon, D. T. Adroja, D. J. Voneshen, Kyoo Kim, T.-H. Jang, J.-H. Park, Kwang-Yong Choi<sup>1</sup> and Sungdae Ji, "Majorana fermions in the Kitaev quantum spin system  $\alpha$ - $\text{RuCl}_3$ ", November 2017, *Nature*, DOI: 10.1038/NPHYS4264
- [9] Sangjun Jeon, Yonglong Xie, Jian Li, Zhijun Wang, Andrei Bernevig, Ali Yazdani<sup>1</sup>, "Distinguishing a Majorana zero mode using spin-resolved measurements", *Science* 358, 772–776 (2017)
- [10] Berthold Jäck<sup>1</sup>, Yonglong Xie, Jian Li, Sangjun Jeon<sup>1</sup>, B. Andrei Bernevig, Ali Yazdani, "Observation of a Majorana zero mode in a topologically protected edge channel", *Science* 364, 1255–1259 (2019)
- [11] Junying Shen<sup>a</sup>, Jian Lyua<sup>a,b</sup>, Jason Z. Gao<sup>a</sup>, Ying-Ming Xie<sup>a</sup>, Chui-Zhen Chen<sup>a</sup>, Chang-woo Choa<sup>a</sup>, Omargeldi Atanova<sup>a</sup>, Zhijie Chen<sup>c</sup>, Kai Li<sup>c</sup>, Yajian J. Hue<sup>c</sup>, King Yau Yip<sup>e</sup>, Swee K. Gohe<sup>e</sup>, Qing Lin Hef<sup>e</sup>, Lei Pan<sup>f</sup>, Kang L. Wang<sup>f</sup>, Kam Tuen Law<sup>a</sup>, and Rolf Lortz<sup>a</sup>, "Spectroscopic fingerprint of chiral Majorana

- modes at the edge of a quantum anomalous Hall insulator/ superconductor heterostructure", 238–242, PNAS, January 7, 2020, vol. 117, no. 1
- [12] Sujit Manna, Peng Weic, Yingming Xied, Kam Tuen Lawd, Patrick A. Leea, and Jagadeesh S. Mooderaa, "Signature of a pair of Majorana zero modes in superconducting gold surface states", PNAS, April 21, 2020, vol. 117, no. 16, 8775–8782
  - [13] Zhang, H., Liu, CX., Gazibegovic, S. et al. RETRACTED ARTICLE: Quantized Majorana conductance. *Nature* 556, 74–79 (2018). <https://doi.org/10.1038/nature26142>
  - [14] Zhang, H., Liu, CX., Gazibegovic, S. et al. Retraction Note: Quantized Majorana conductance. *Nature* 591, E30 (2021). <https://doi.org/10.1038/s41586-021-03373-x>
  - [15] Hao-Hua Sun, Jin-Feng Jia, "Majorana zero mode in the vortex of artificial topological superconductor", February 2017, DOI: <https://doi.org/10.1007/s11433-017-9011-7>
  - [16] Hao-Hua Sun and Jin-Feng Jia, "Detection of Majorana zero mode in the vortex", *npj Quantum Materials* (2017)2:34; doi:10.1038/s41535-017-0037-4
  - [17] Caroli, C., de Gennes, P. G., and Matricon, J. (1964). Bound Fermion States on a Vortex Line in a Type II Superconductor. *Physics Letters*, 9(4), 307–309. [https://doi.org/10.1016/0031-9163\(64\)90375-0](https://doi.org/10.1016/0031-9163(64)90375-0)
  - [18] Microsoft Corporation, "Microsoft unveils Majorana 1, the world's first quantum processor powered by topological qubits," Feb. 19, 2025. [Online]
  - [19] Microsoft Azure Quantum et al., 19 February 2025, Interferometric single-shot parity measurement in InAs–Al hybrid devices, *Nature*, 651–655 (2025)
  - [20] B.D. Josephson, 'Possible new effects in superconductive tunnelling', July 1, 1962, [https://doi.org/10.1016/0031-9163\(62\)91369-0](https://doi.org/10.1016/0031-9163(62)91369-0)
  - [21] Chun-Xiao Liu, Bernard van Heck, Michael Wimmer, 'Josephson current via an isolated Majorana zero mode', January 14, 2023, *Physical Review B*, <https://arxiv.org/pdf/2005.10657>
  - [22] Tom Dvir, Guanzhong Wang, Nick van Loo, Chun-Xiao Liu, Grzegorz P. Mazur, Alberto Bordin, Sebastiaan L. D. ten Haaf, Ji-Yin Wang, David van Driel, Francesco Zatelli, Xiang Li, Filip K. Malinowski, Sasa Gazibegovic, Ghada Badawy, Erik P. A. M. Bakkers, Michael Wimmer and Leo P. Kouwenhoven "Realization of a minimal Kitaev chain in coupled quantum dots", *Nature*, Vol614, 16February2023
  - [23] Kitaev, A. Y. (2001). Unpaired Majorana fermions in quantum wires. *Physics-Uspekhi*, 44(10S), 131-136.
  - [24] Munkres, J. R. (2000). *Topology* (2nd ed.). Prentice Hall.
  - [25] Bethe, H. A., Salpeter, E. E. (1957). Quantum Mechanics of One- and Two-Electron Atoms. In *Handbuch der Physik / Encyclopedia of Physics*, Volume 35: Quantum Mechanics of Atoms and Molecules (pp. 93-220).

- [26] C. W. J. Beenakker, "Random-matrix theory of quantum transport," *Rev. Mod. Phys.* 69, 731 (1997). <https://www.arxiv.org/abs/cond-mat/9612179>
- [27] A. Altland and B. D. Simons, "Condensed Matter Field Theory," Cambridge University Press, 2010. pg 272.
- [28] Nayak, C., Tewari, S., Sarma, S. D. (2006). Majorana Fermions and Non-Abelian Statistics in Three Dimensions. *Physical Review Letters*, 94(4), 040502.
- [29] Holstein, T. "Studies of polaron motion: Part I. The fundamental equations." *Annals of Physics* 8.3 (1959): 343-389.
- [30] Kittel, Charles. *Introduction to Solid State Physics*, 8th Edition. Wiley, 2005. Chapter 12.
- [31] Martin R. Zirnbauer. Particle-Hole Symmetries in Condensed Matter. *J. Math. Phys.* 62 (2021) 021101. pg 11.
- [32] Reif, F. (1965). *Fundamentals of Statistical and Thermal Physics*. McGraw-Hill.
- [33] Domb, C., Green, M. S. (1974). *Phase Transitions and Critical Phenomena* (Vol. 3, pp. 1-76). Academic Press.
- [34] Ying, T., Guo, H., et al. (2024). Charge density wave and pairing order in the Holstein model on the honeycomb lattice away from half-filling. *Physical Review B*, 110(20), 205145. <https://doi.org/10.1103/PhysRevB.110.205145>
- [35] Peierls, R., 1955. Quantum theory of solids. *Physica*, 20(1-6), pp.989-1000.
- [36] Grüner, G. (1988). The dynamics of charge-density waves. *Reviews of Modern Physics*, 60(4), 1129-1181. <https://doi.org/10.1103/RevModPhys.60.1129>
- [37] Jinwoong Hwang et al 2024 *Rep. Prog. Phys.* 87 044502; DOI: 10.1088/1361-6633/ad36d3; <https://iopscience.iop.org/article/10.1088/1361-6633/ad36d3>
- [38] L. Benfatto, A. Toschi and S. Caprara. (28 May 2004). Low-energy phase-only action in a superconductor: A comparison with the XY model. *Phys. Rev. B* 69, 184510. <https://doi.org/10.1103/PhysRevB.69.184510>
- [39] Matsubara, T. (1955). A new approach to quantum-statistical mechanics. *Progress of Theoretical Physics*, 14(4), 351-378. <https://doi.org/10.1143/PTP.14.351>
- [40] Fetter, A. L. and Walecka, J. D. (1971). *Quantum Theory of Many-Particle Systems*. McGraw-Hill.
- [41] Maxwell, J. C. (1875). On the Dynamical Evidence of the Molecular Constitution of Bodies. *Philosophical Transactions of the Royal Society of London*, 170, 231-256.